Supplementary Materials for

Hydrogen-Bond-Engineered Polymer Dielectrics for 250 °C Operation Enabled by Deep-Learning-Based Virtual Screening

Jinfeng Li[1,2], Tao Lu[1,2], Ruize Wang[1,2], Shiqi Wang[1,2], Wei Jiang[3], Binhan Lv[4], Yan Gao[5]*, Tian Zhang[1,2]**

[1]Electronic Information School, Wuhan University, Wuhan 430072, P. R. China.

[2]Suzhou Institute of Wuhan University, Suzhou 215000, P. R. China.

[3]School of Materials Science and Engineering, Jilin University of Chemical Technology, Jilin 132022, China.

[4]College of Chemistry and Pharmaceutical Engineering, Jilin University of Chemical Technology, Jilin 132022, P. R. China.

[5]Centre of Analysis and Measurement, Jilin University of Chemical Technology, Jilin 132022, P. R. China.

*e-mail: gyaxz@126.com

**e-mail: txz908@whu.edu.cn

The PDF file includes:

Supplementary Text
Figs. S1 to S21
Tables S1 to S5

Contents

1. Deep Learning

Computation of molecular surfaces. All polymer candidate structures were obtained from the First Principles Dataset (Dataset S1) and the PolyInfo Database (Dataset S2). Three-dimensional electrostatic potential (ESP) maps for each molecule were first generated using Density Functional Theory (DFT) calculations at the B3LYP/6-31G* level. These 3D ESP maps were subsequently transformed into atom-based 2D molecular graph structures, where nodes represent atoms and edges represent chemical bonds or spatial proximities.

Each atom node was assigned a vector of key physico-chemical features for subsequent graph neural network learning:

Electrostatic potential (ESP) value, identifying regions of positive and negative potential critical for hydrogen-bond formation.

Hydrogen-bond donor and acceptor propensity, quantified via local atom types (e.g., N, O – H donors; O, N acceptors) and their spatial distribution.

HOMO-LUMO energy levels, for evaluating electronic structure and bandgap.

Predicted hydrogen-bond probability and binding energy, with initial estimates derived from preliminary analysis of DFT-computed data.

Equilibrium bond length, incorporated as geometric constraint information.

These features were integrated into a graph deep learning framework specifically designed for molecular graph structures, processed by a Graph Neural Network (GNN) to simultaneously predict multiple target properties.

Deep learning framework for hydrogen-bond interaction prediction. We employed a Graph Neural Network (GNN) to model the complex mapping between molecular graph structures and target properties. Since molecular graphs are irregular, non-Euclidean data structures, we utilized message-passing mechanisms to capture the local chemical environment between atoms. Within this framework, each node updates its own feature representation by aggregating information from its neighboring nodes, thereby learning a global representation of the entire molecule.

Network architecture and training. The network input is the complete molecular graph containing all atom nodes and chemical bond edges. Each node contains a six-dimensional feature vector encompassing the aforementioned ESP, donor/acceptor propensity, HOMO-LUMO levels, hydrogen-bond probability, binding energy, and bond length.

The core network architecture consists of the following components:

Graph Convolutional Layers (message-passing layers) for propagating and aggregating chemical features within atomic neighborhoods.

A Global Attention Pooling layer that aggregates feature from all nodes into a single feature vector representing the entire molecule.

A Multi-task Regression Output layer that maps this global feature vector simultaneously to four key target properties: hydrogen bond probability (Pbind), hydrogen bond energy (Δ Gbind), the number of hydrogen bonds per monomer unit, and the electronic bandgap (E_g).

Training strategy and loss function. The model was trained in a supervised manner on a training set comprising 1,000 polymer structures, and its performance was evaluated on a separate test set of 200 structures. The training objective was to minimize a multi-task Mean Squared Error (MSE) loss function, which concurrently measures the discrepancy between the four predicted targets and their DFT reference values.

The model was trained using the Adam optimizer (learning rate 1×10^{-4}), and early stopping was employed to prevent overfitting. With this training strategy, the model achieved a mean absolute error (MAE) of less than 0.05 eV for bandgap (E_g) prediction and less than 0.5 kJ/mol for binding energy (Δ Gbind) prediction on the test set, demonstrating excellent predictive accuracy and generalization capability.

Selection of optimal candidates. During the prediction phase, the trained GNN model was used to compute the four target properties for all candidate polymers. Candidates were ranked based on the following combined criteria: high hydrogen bond probability (Pbind > 0.8), strong binding energy (Δ Gbind > 20 kJ/mol), the total number of hydrogen bonds in the simulation cell normalized per monomer unit (NHB > 300), and wide bandgap (E_g > 4.0 eV). Ultimately, the three top-performing polymers, denoted as T-FB, O-MP and O-PU were selected for subsequent experimental synthesis and validation.

Table S1. DFT calculations for validation set structures.

Num -ber	Structure	ESP	Homo Lumo	Band Gap (eV)
1	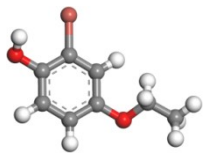	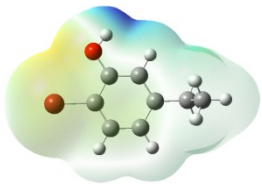	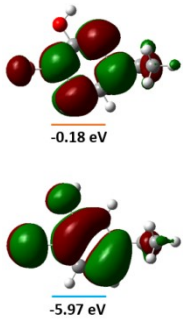	**5.78 eV**
2	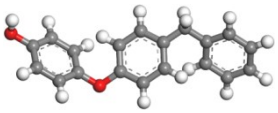	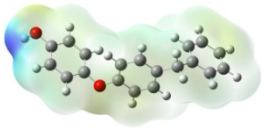	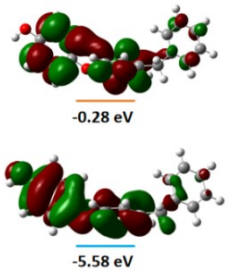	**5.30 eV**
3	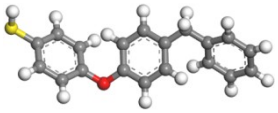	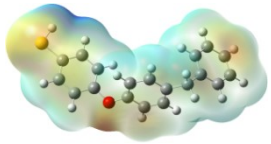	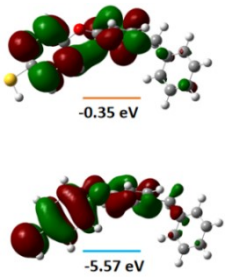	**5.22 eV**
4	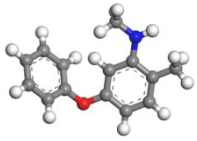	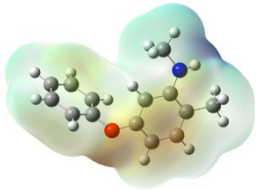	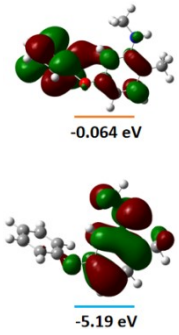	**5.12 eV**

5	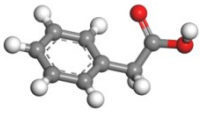	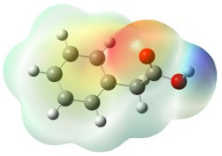	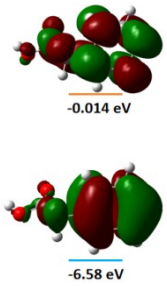	**6.57 eV**
6	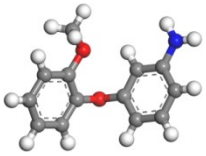	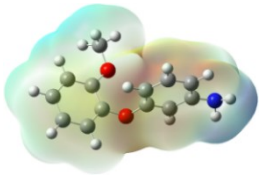	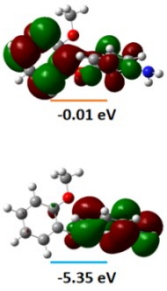	**5.34 eV**
7	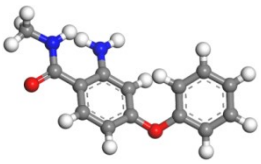	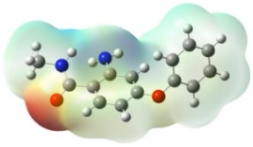	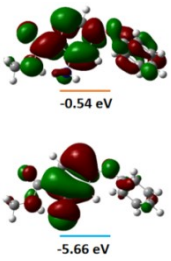	**5.12 eV**
8	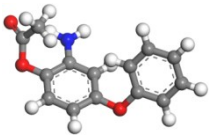	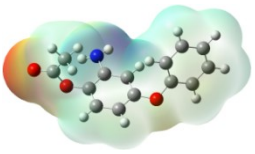	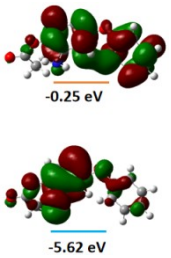	**5.37 eV**
9	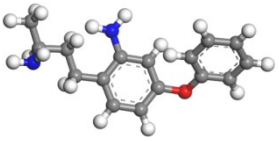	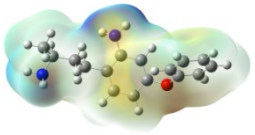	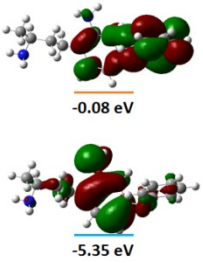	**5.28 eV**

10	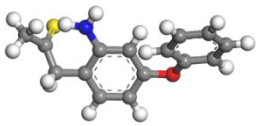	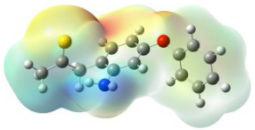	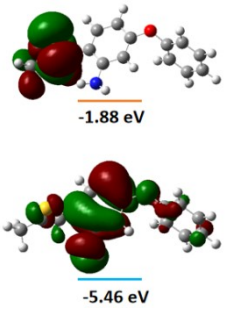	**3.58 eV**
11	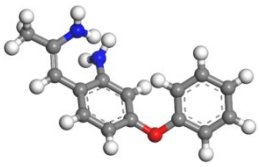	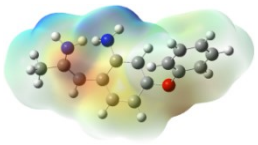	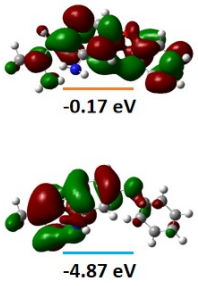	**4.70 eV**
12	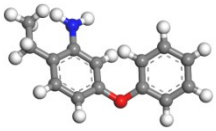	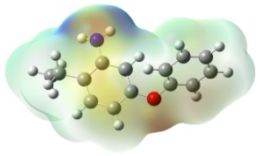	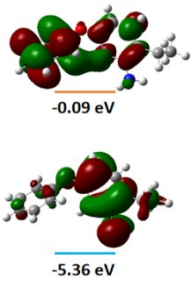	**5.27 eV**
13	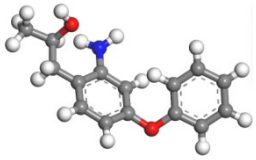	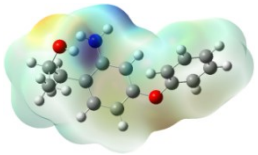	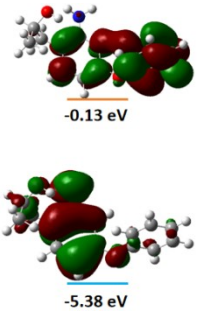	**5.24 eV**
14	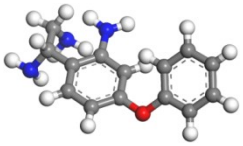	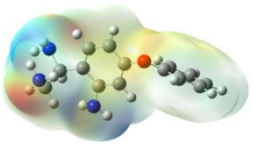	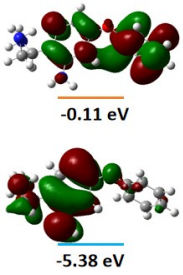	**5.27 eV**

15	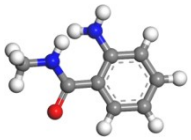	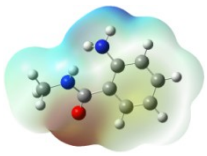	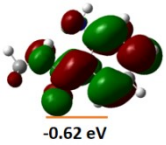 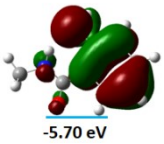	**5.08 eV**
16	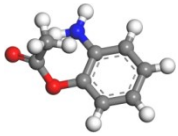	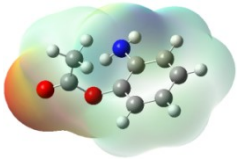	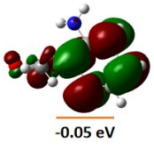 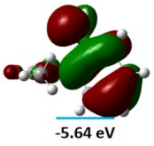	**5.59 eV**
17	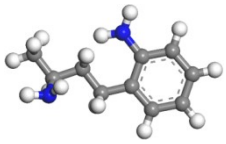	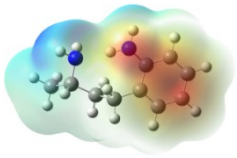	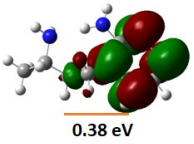 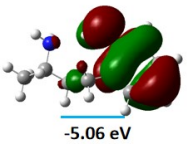	**5.44 eV**
18	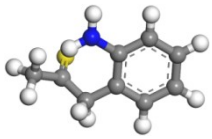	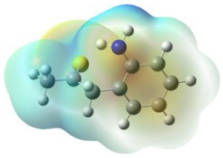	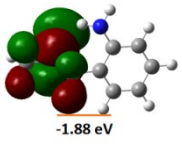 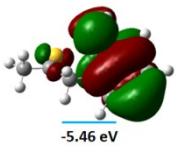	**3.59 eV**
19	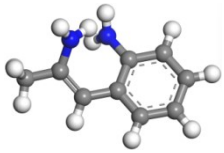	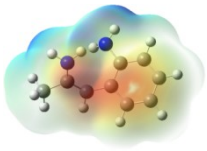	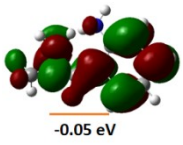 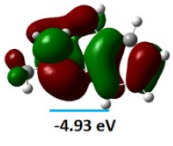	**4.88 eV**

20	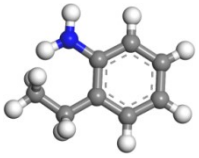	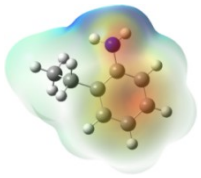	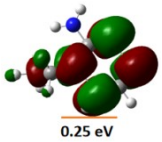 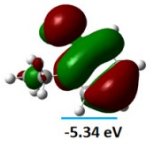	**5.60 eV**
21	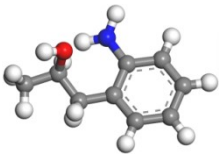	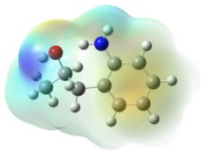	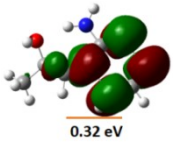 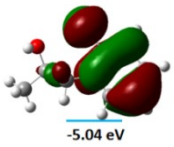	**5.35 eV**
22	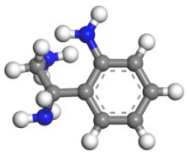	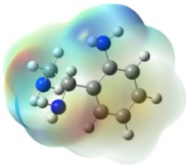	 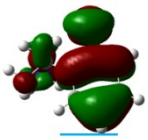	**5.58 eV**
23	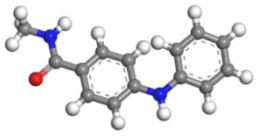	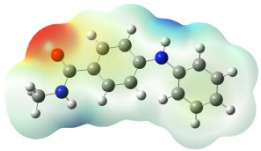	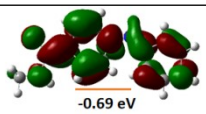 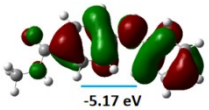	**4.48 eV**
24	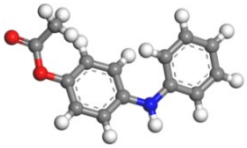	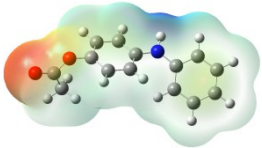	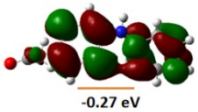 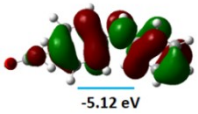	**4.85 eV**

25	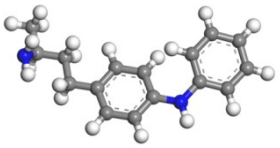	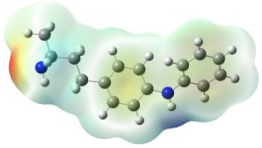	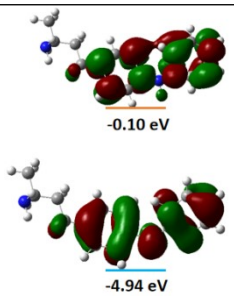	**4.85 eV**
26	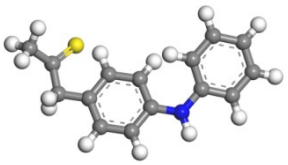	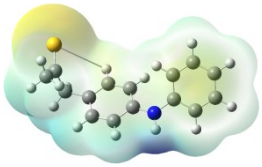	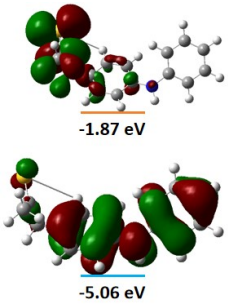	**3.19 eV**
27	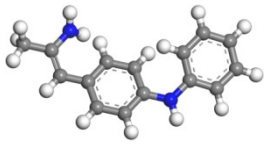	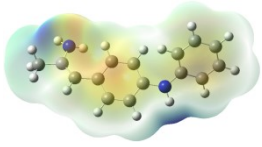	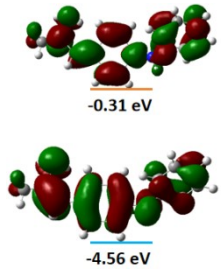	**4.25 eV**
28	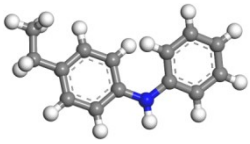	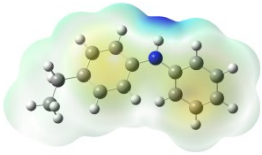	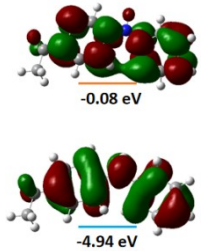	**4.86 eV**
29	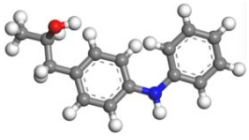	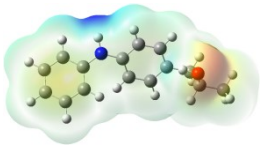	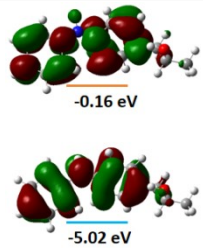	**4.86 eV**
30	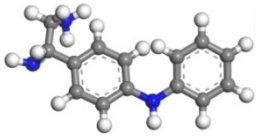	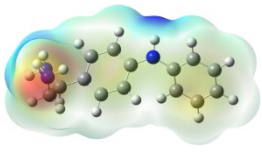	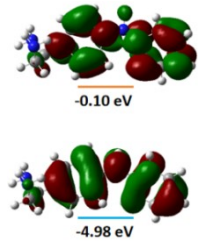	**4.88 eV**

31	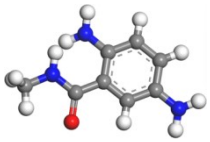	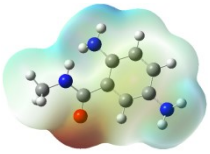	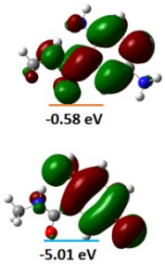	**4.43 eV**
32	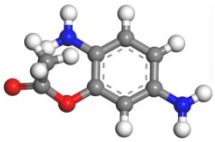	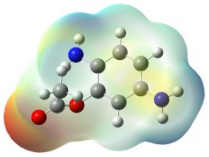	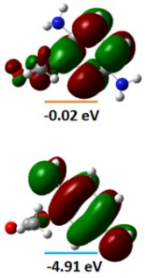	**4.89 eV**
33	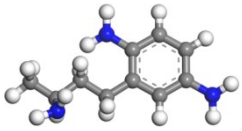	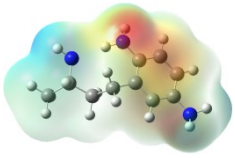	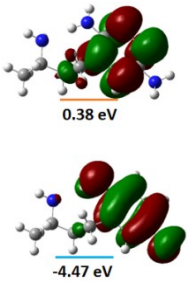	**4.84 eV**
34	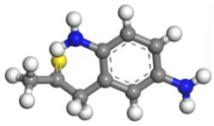	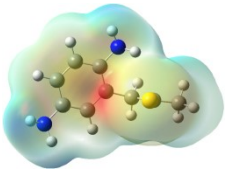	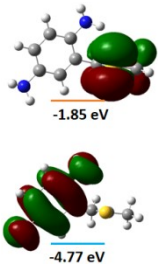	**2.92 eV**
35	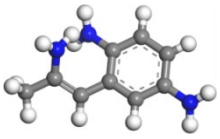	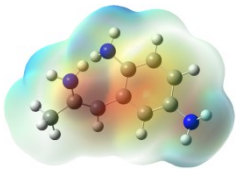	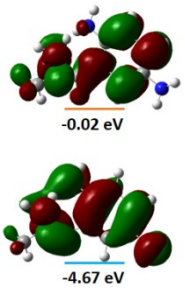	**4.64 eV**

36	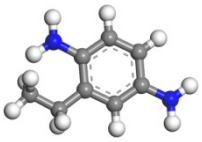	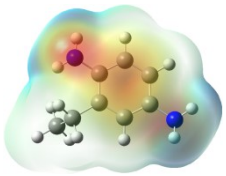	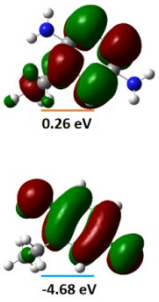	**4.94 eV**
37	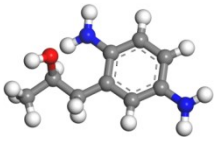	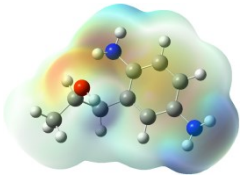	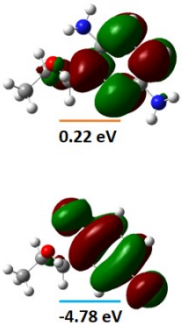	**5.00 eV**
38	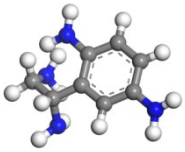	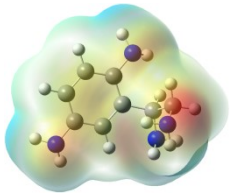	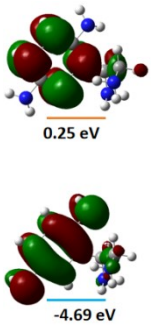	**4.94 eV**
39	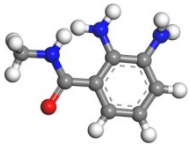	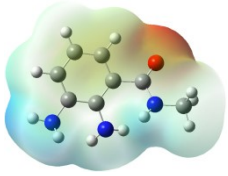	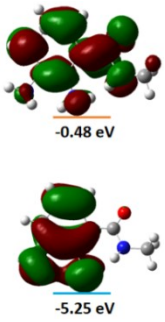	**4.77 eV**
40	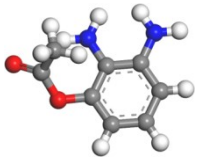	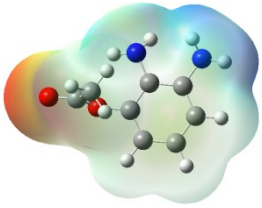	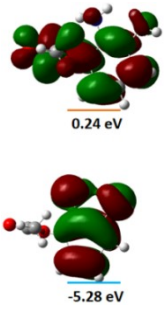	**5.52 eV**

41	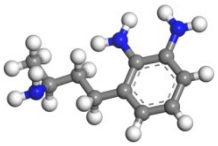	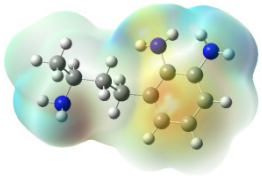	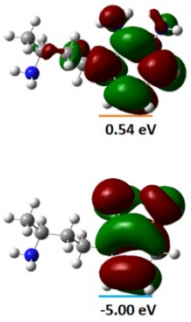	**5.54 eV**
42	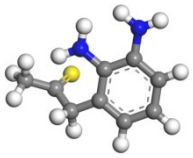	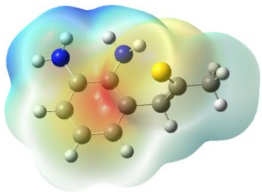	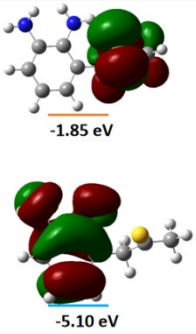	**3.25 eV**
43	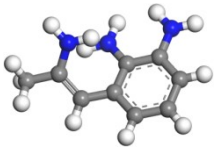	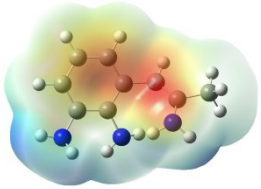	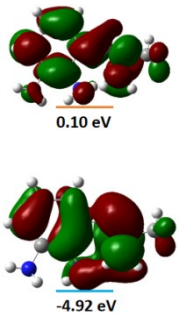	**5.02 eV**
44	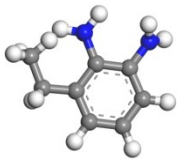	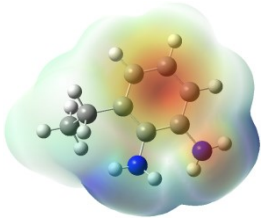	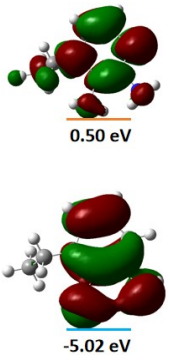	**5.52 eV**
45	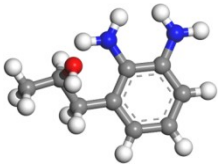	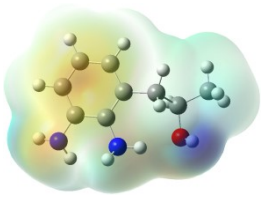	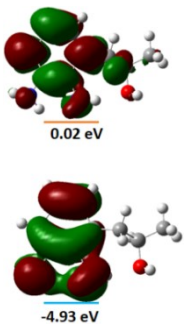	**5.40 eV**

46	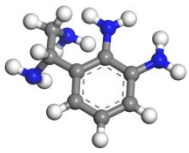	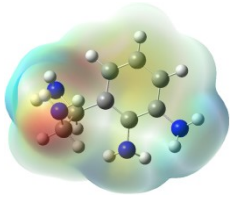	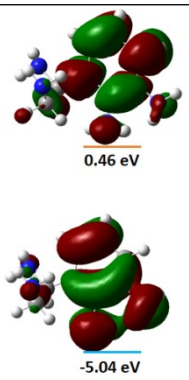	**5.50 eV**
47	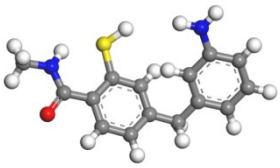	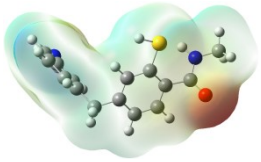	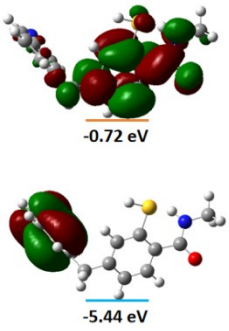	**4.72 eV**
48	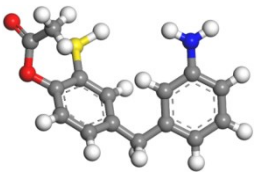	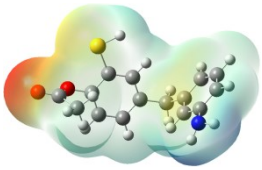	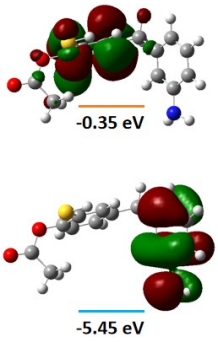	**5.10 eV**
49	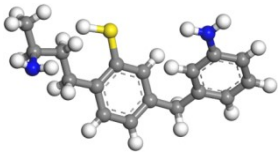	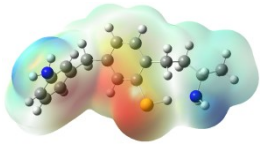	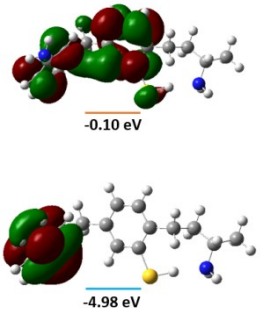	**5.42 eV**

50	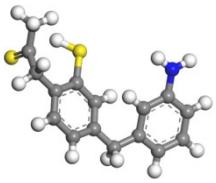	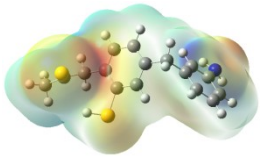	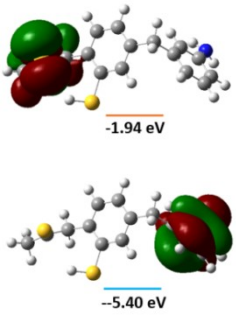	**3.46 eV**
51	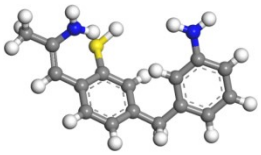	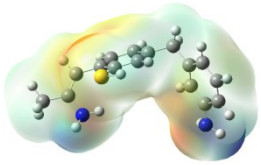	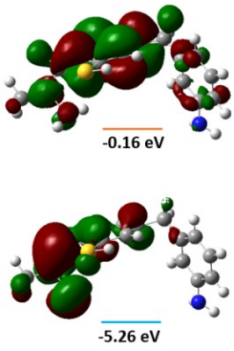	**5.10 eV**
52	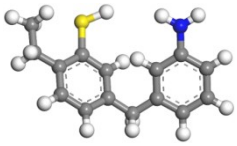	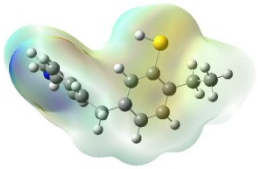	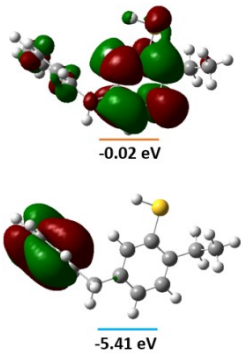	**5.39 eV**
53	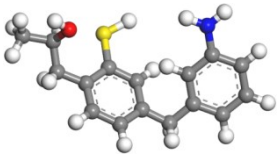	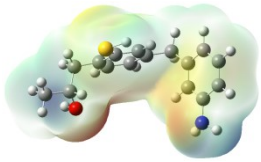	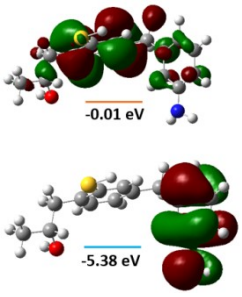	**5.36 eV**

54	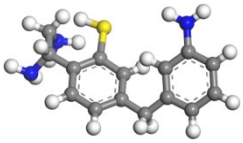	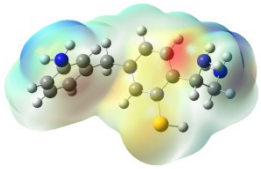	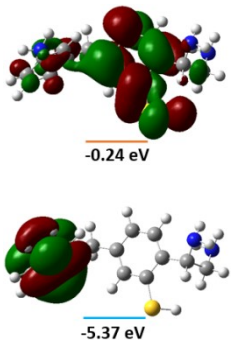	**5.13 eV**
55	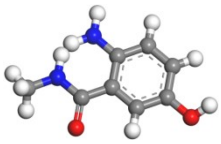	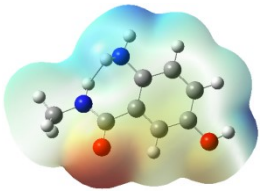	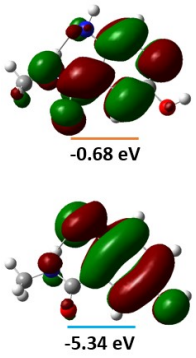	**4.66 eV**
56	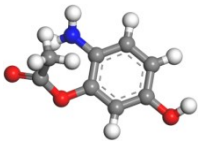	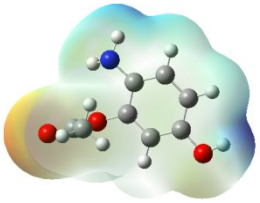	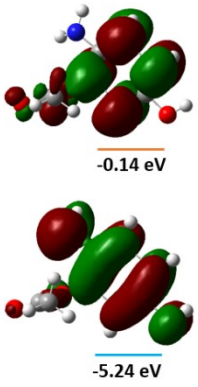	**5.09 eV**
57	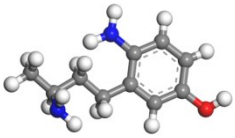	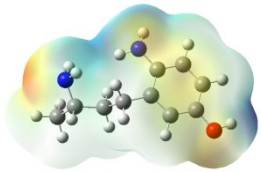	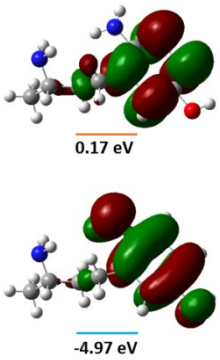	**5.14 eV**

58	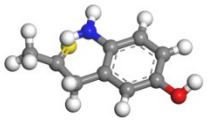	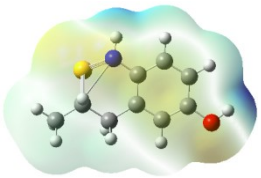	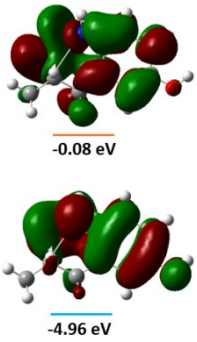	**4.87 eV**
59	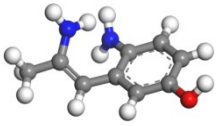	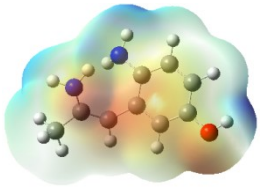	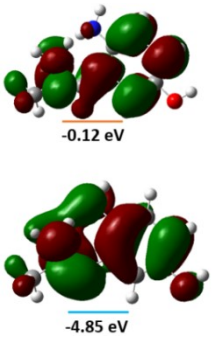	**4.73 eV**
60	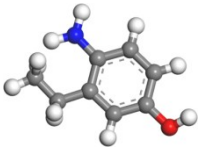	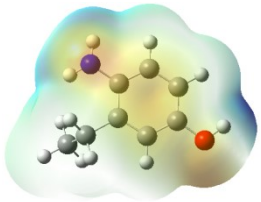	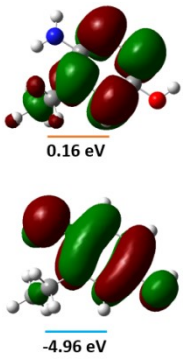	**5.12 eV**
61	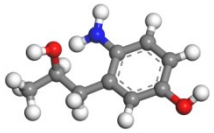	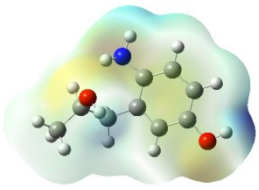	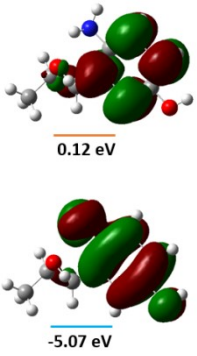	**5.19 eV**

62	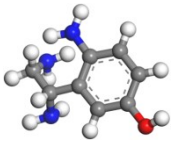	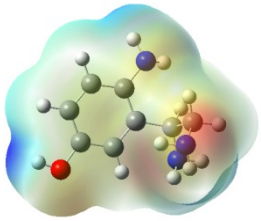	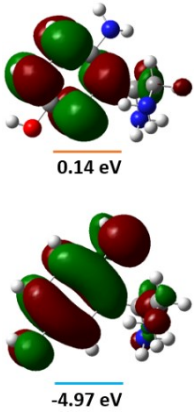	**5.11 eV**
63	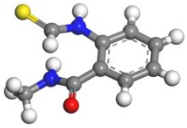	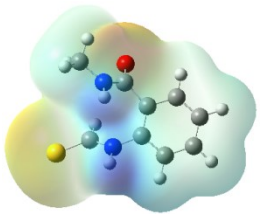	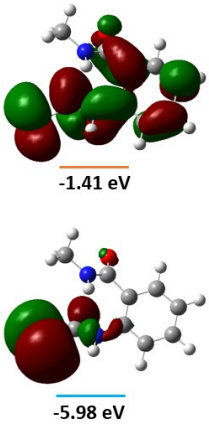	**4.57 eV**
64	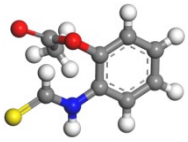	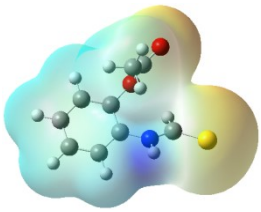	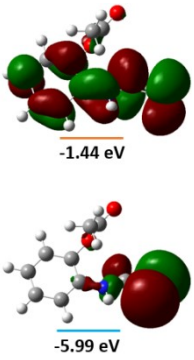	**4.55 eV**
65	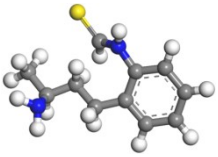	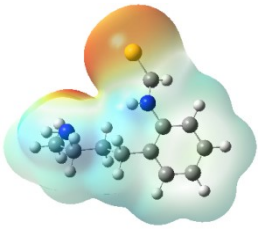	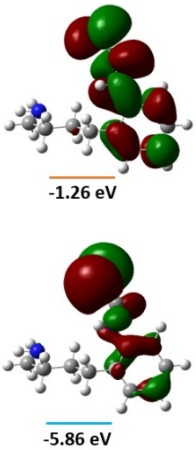	**4.59 eV**

66	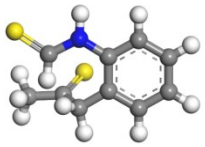	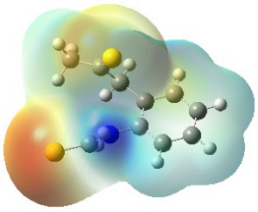	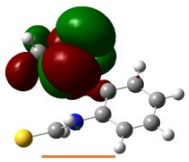 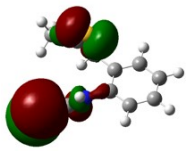	**4.00 eV**
67	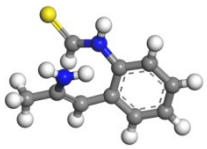	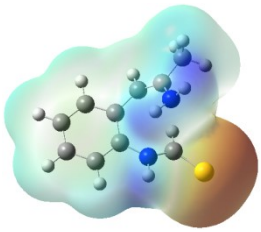	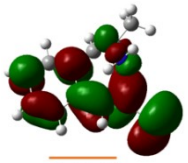 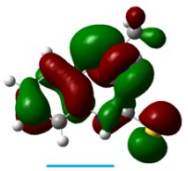	**4.00 eV**
68	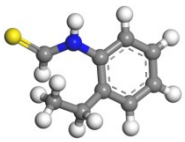	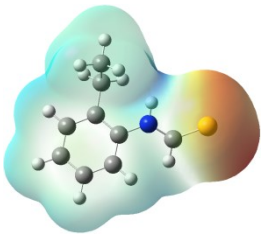	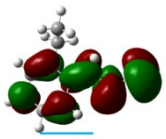 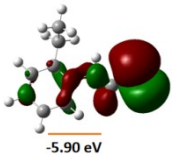	**4.62 eV**
69	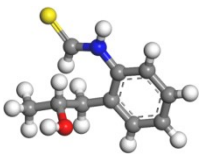	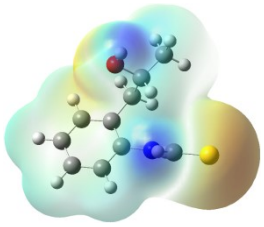	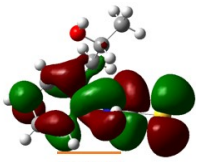 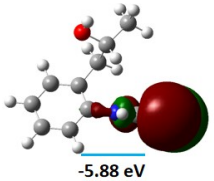	**4.79 eV**

70	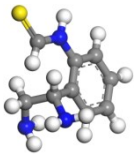	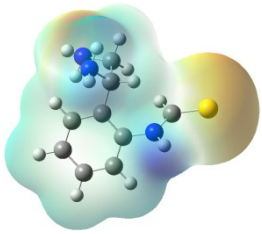	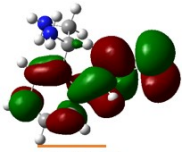 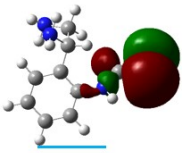	**4.77 eV**
71	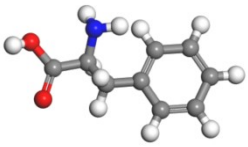	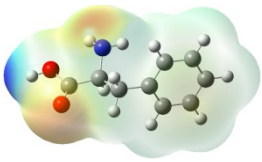	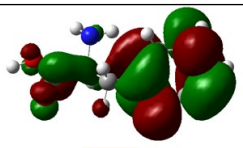 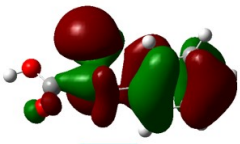	**6.43 eV**
72	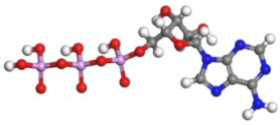	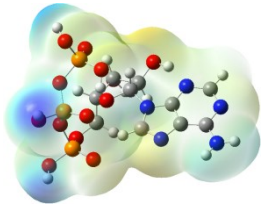	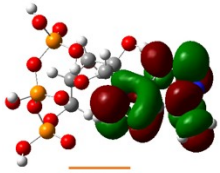 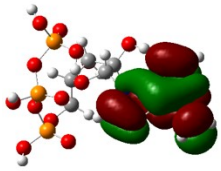	**5.38 eV**
73	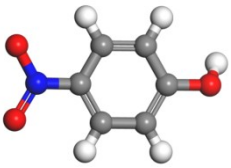	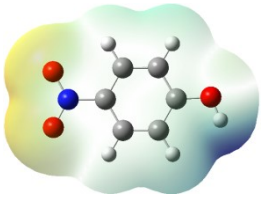	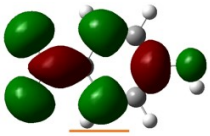 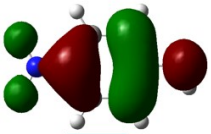	**4.43 eV**

74	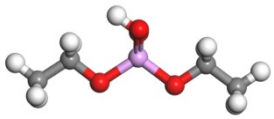	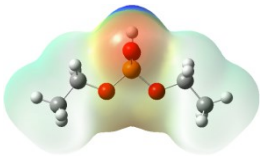	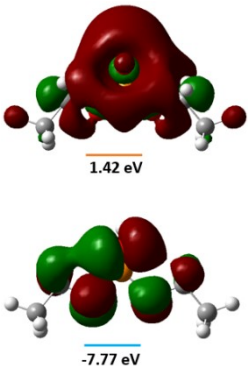	**9.20 eV**
75	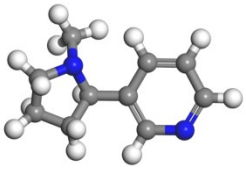	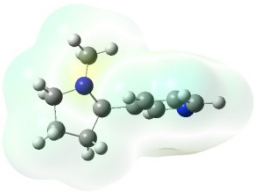	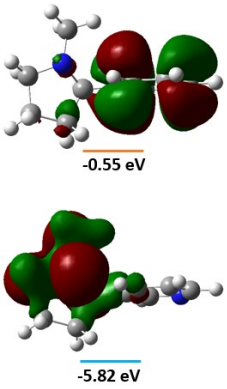	**5.27 eV**
76	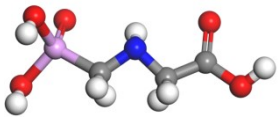	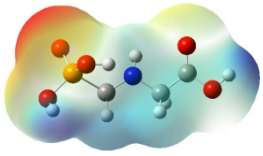	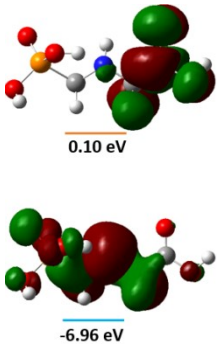	**7.06 eV**
77	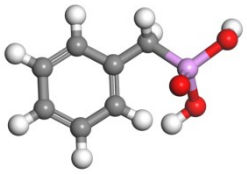	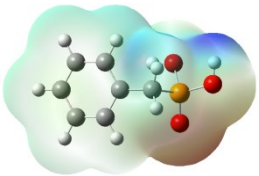	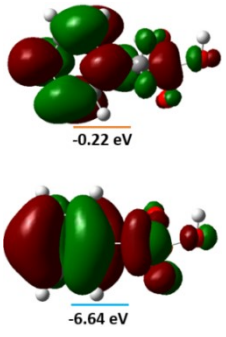	**6.43 eV**

78	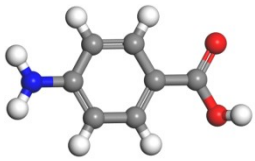	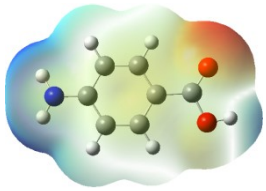	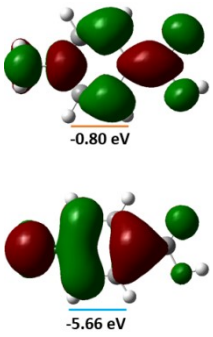	**4.86 eV**
79	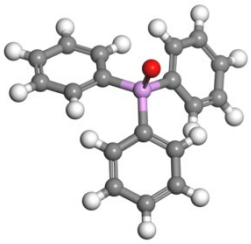	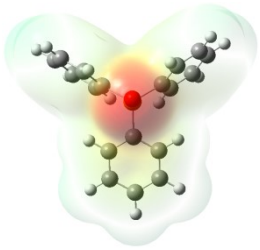	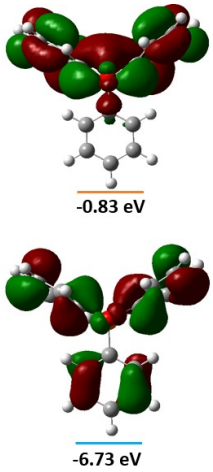	**5.90 eV**
80	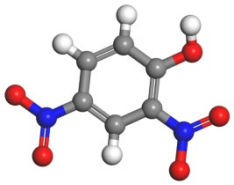	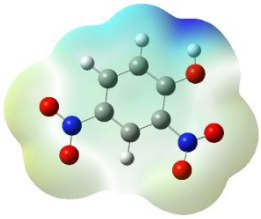	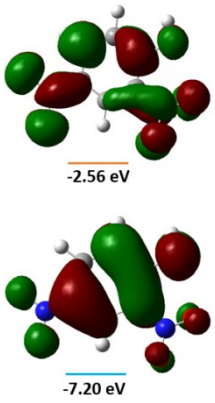	**4.64 eV**
81	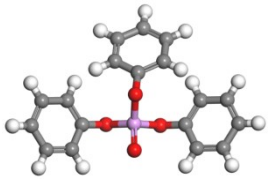	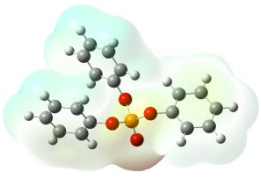	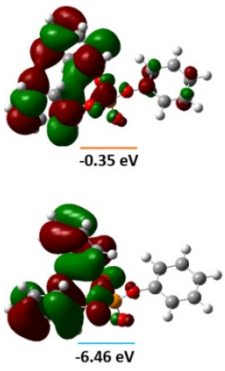	**6.11 eV**

82	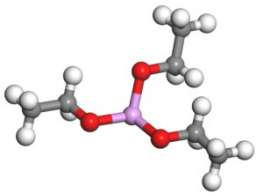	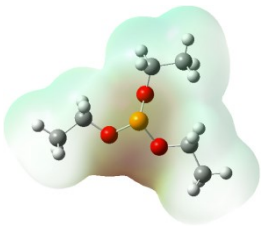	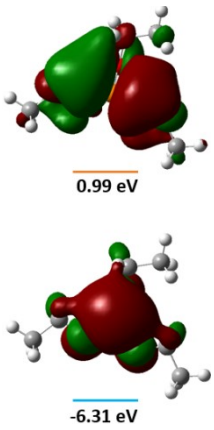	**7.30 eV**
83	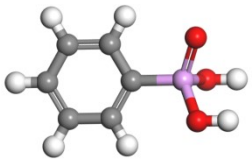	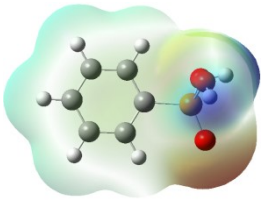	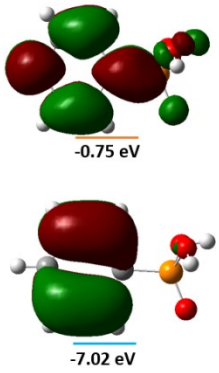	**6.27 eV**
84	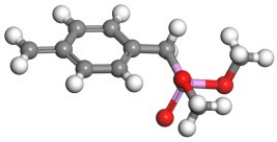	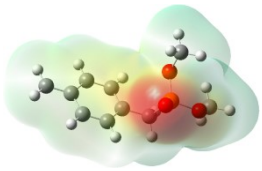	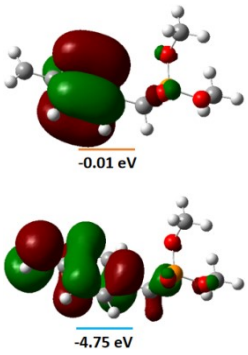	**4.74 eV**
85	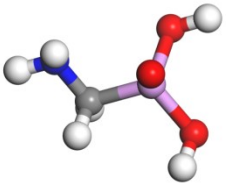	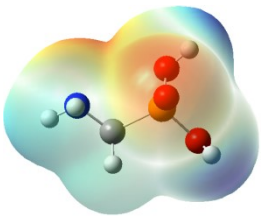	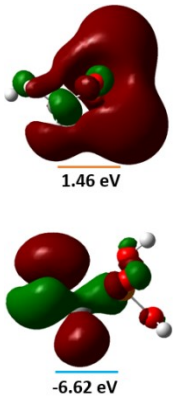	**8.07 eV**

86	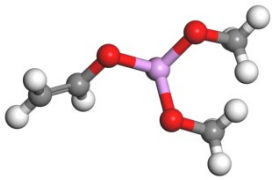	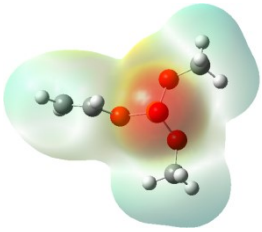	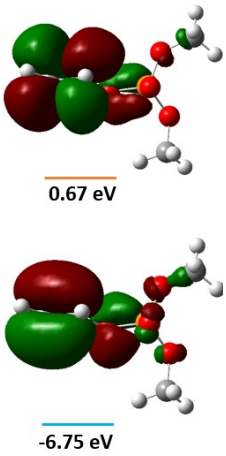	**7.42 eV**
87	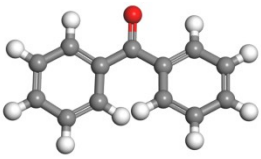	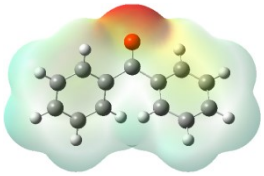	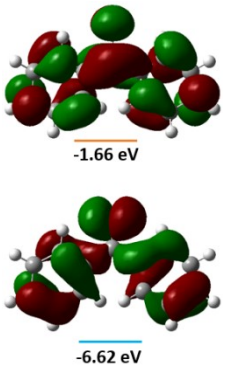	**4.96 eV**
88	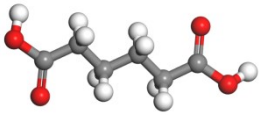	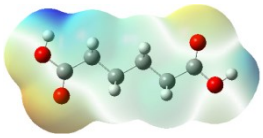	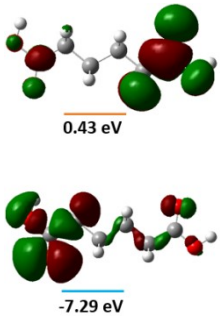	**7.72 eV**
89	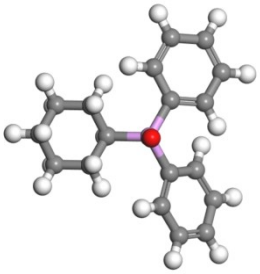	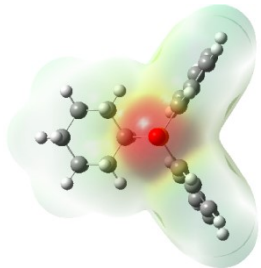	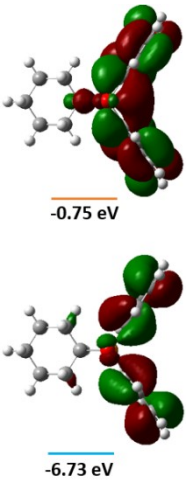	**5.97 eV**

90	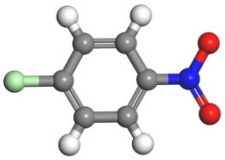	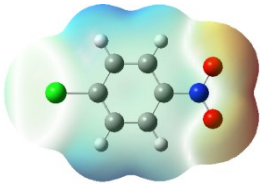	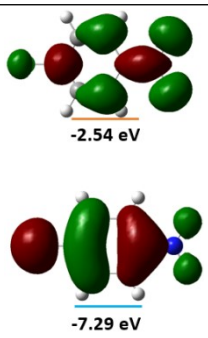	**4.75 eV**
91	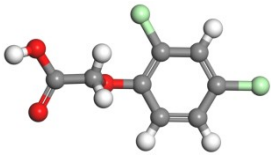	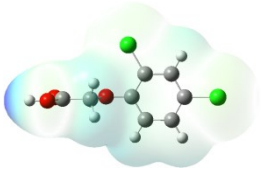	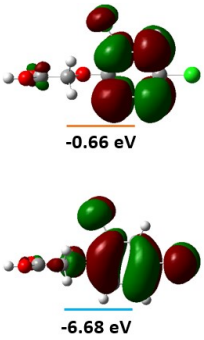	**6.02 eV**
92	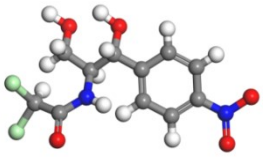	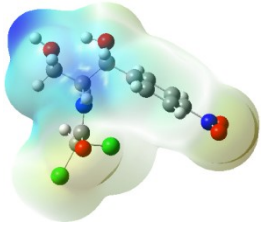	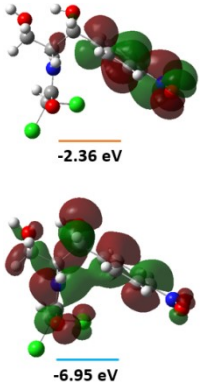	**4.60 eV**
93	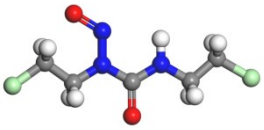	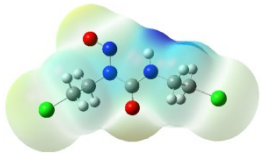	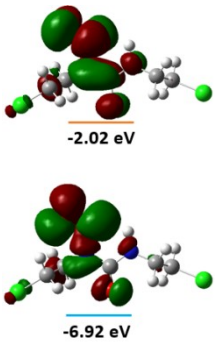	**4.90 eV**

94	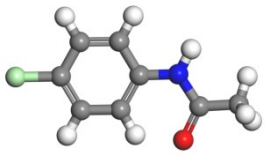	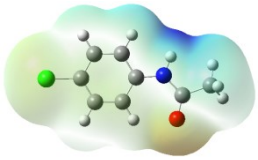	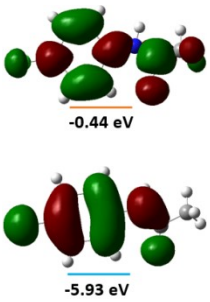	**5.50 eV**
95	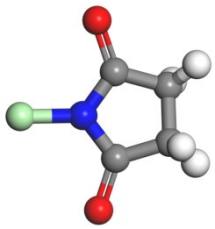	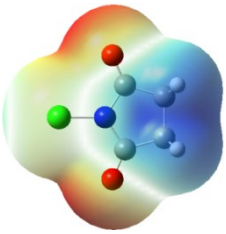	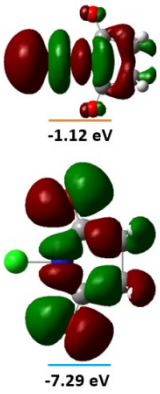	**6.17 eV**
96	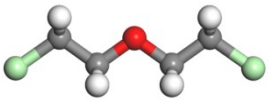	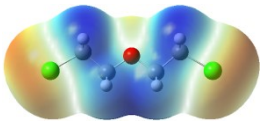	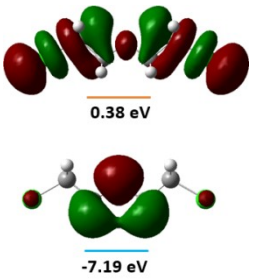	**7.57 eV**
97	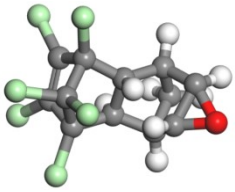	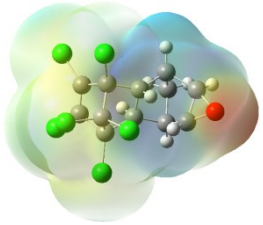	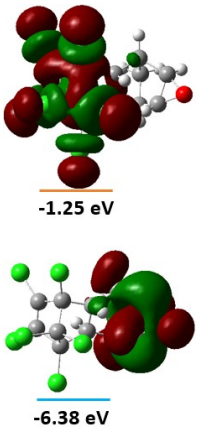	**5.13 eV**

98	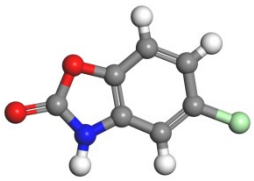		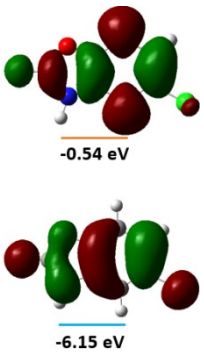	**5.61 eV**
99	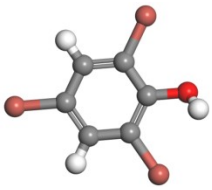	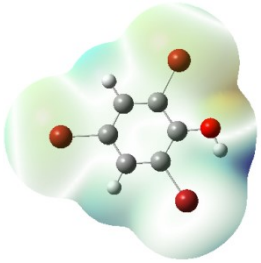	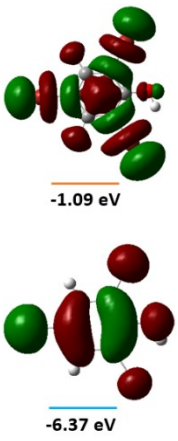	**5.29 eV**
100	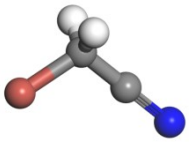	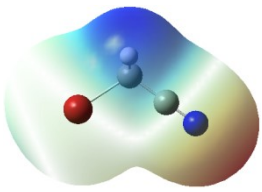	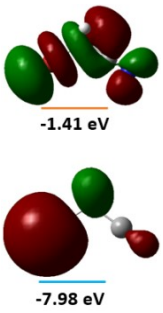	**6.56 eV**

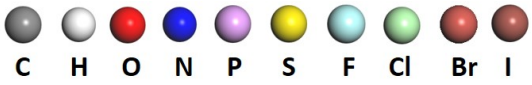

2. Molecular dynamics simulation

2.1 Theoretical background

In this work we focus on calculation of ε_r, so we omit the subscript "r" in the following. In general, permittivity is a complex and frequency-dependent quantity,

$$\varepsilon(w) = \varepsilon_1(w) - \varepsilon_2(w) \quad (1)$$

where ε_1 and ε_2 are real and ε_2 is the dielectric loss. In anisotropic materials, permittivity is a complex tensor that depends on the orientations of the field and the sample. The elements of the static permittivity tensor $\varepsilon_{\alpha\beta}$ (0) have both electronic and ionic contributions, which can be expressed as[S1-S5]:

$$\varepsilon_{\alpha\beta}(0) - \varepsilon_{\alpha\beta}(\infty) = \frac{4\pi}{\Omega k_B T} \mathrm{M}_{\alpha\beta} \quad (2)$$

where α and β stand for the three Cartesian directions, $\varepsilon_{\alpha\beta}(\infty)$ is the electronic dielectric constant, Ω is the volume of simulation supercell, k_B is the Boltzmann constant, and T is temperature. $\mathrm{M}_{\alpha\beta}$ is the covariance of two dipole moment components,

$$M_{\alpha\beta} = \langle M_\alpha M\beta\rangle - \langle M\alpha\rangle\langle M\beta\rangle \quad (3)$$

In molecular dynamics (MD) simulation with charged atoms, $\mathrm{M}\alpha = \sum_i q_i r_{i\,\alpha}$ is the dipole moment in the α direction, q_i is the charge, and $r_{i\,\alpha}$ is the α coordinate of atom i. The summation is over all atoms in the simulation cell. The dipole moment M can be obtained from MD simulation in the canonical ensemble. The frequency-dependent permittivity $\varepsilon_{\alpha\beta}(w)$ can then be extracted by Fourier transforming the cross covariance of time-dependent dipole moments.

$$\in_{\alpha\beta}(w) = \in_{\alpha\beta}(0) - \frac{4\pi}{\Omega k_B T} iw \int_0^\infty e^{-iwt} M_{\alpha\beta}(t)dt \quad (4)$$

Where $M_{\alpha\beta}(t)$= $\langle M_{\alpha}(0)M_{\beta}(t)\rangle$ - $\langle M_{\alpha}\rangle$ $\langle M_{\beta}\rangle$. The imaginary part of $\varepsilon_{\alpha\beta}(w)$ is the loss.

2.2 Computational details

2.2.1 Modeling construction

To simulate the self-adaptability of the multisite bonding network in the polymers, models of PI, O-PU, and O-PU/PI were constructed. Since the degree of polymerization has limited effects on the simulation process in these polymers[S6-S7], to improve simulation efficiency a chain number of 4 and a repeating unit of 10 were chosen for the PI polymer model, resulting in a simulation box size of 32.8 × 32.8 × 32.8 $Å^3$. While the O-PU/PI composite model, with 15% O-PU content, was set at 35.2 × 35.2 × 35.2 $Å^3$. The proportions of PI and O-PU in the polymer models were selected based on the optimal experimental conditions. To ensure that the models reached equilibrium and relieved any internal stresses, each underwent 10,000 steps of energy minimization followed by at least 1000 ps of molecular dynamics (MD) simulation. This simulation was conducted using the COMPASS force field under an NPT (possessing a certain number of particles (N), pressure (P), and temperature (T) ensemble) ensemble with a constant pressure of 0.0001 GPa, temperature of 300 K, and a time step of 1.0 fs. Free volume simulation is calculated by this condition.

2.2.2 Molecular dynamics simulation based on reaction force field (ReaxFF-MD)

ReaxFF is a force field for reactions that rely on classical mechanical equations and incorporates insights from various empirical force fields to postulate bond order. Within the ReaxFF framework, the notion of bond order serves to ascertain atomic connectivity, thereby depicting bond formation and dissociation. A fundamental presumption underlying the definition of bond order is the existence of a defined mathematical correlation between bond order and interatomic distance. By measuring

the distance between atoms, the bond order between any given pair can be directly determined. The interplay between atoms is represented through a potential energy function, with updates to atomic states hinging on the ReaxFF potential energy file function—essentially, the force field file parameter.

In the reactive force field (ReaxFF), there are no fixed atomic types, and atoms within the same molecule are not connected by rigid chemical bonds. Instead, their connectivity is dynamically determined by evaluating the bond order between atom pairs. During reactive molecular dynamics simulations, the bond order fluctuates, allowing chemical bonds to form and break continuously. This dynamic process leads to an ongoing update of the bonding characteristics or atomic connectivity within the system. Bond order, therefore, is the critical parameter in ReaxFF, dictating the interactions between atoms. The forces governing these interactions are expressed as a function of bond order, which evolves in response to the molecular environment. In contrast to classical force fields where interactions encompass bonds, bond angles, dihedral angles, conjugations, Coulombic forces, and van der Waals forces, the total energy of the system in the reaction force field is represented as follows[S8]:

$$E_{system} = E_{bond} + E_{lp} + E_{over} + E_{under} + E_{val} + E_{pen} + E_{coa} + E_{C2} + E_{triple} + E_{tors} + E_{conj} + E_{H\text{-}bond} + E_{vdWaals} + E_{Coulomb} \quad (5)$$

Where E_{system} represents the total energy of the system, and energy terms such as E_{bond}, E_{over}, E_{under}, E_{val}, E_{tor}, E_{lp}, $E_{H\text{-}bond}$, $E_{vdwaals}$, and $E_{coulomb}$ are ascribed to the bond energy, energy correction term for under coordination, energy correction term for over coordination, valence angle energy, torsion angle energy, lone pair energy, hydrogen bond energy, van der waals energy, and coulomb energy, respectively. The hydrogen bonds information was examined through simulations conducted using the classical MD code, Large-scale Atomic/Molecular Massively Parallel Simulator (LAMMPS), along with force field ReaxFF. To obtain microscopic structures, we employ a simulated annealing process: starting with a 1 ns equilibration at 600 K within the NPT ensemble, followed by cooling to 300 K at a rate of 25 K per 100 ps, and ending with

another 1 ns equilibration at 300 K in the NPT ensemble. Temperature and pressure are regulated using the Nose-Hoover thermostat, with a target pressure of 0.0001 GPa. The ReaxFF-MD simulation maintains a constant time step of 0.5 fs. Our simulation cell comprises ten independent polymer chains, each consisting of four repeating units, extending periodically throughout the system. PI and O-PU are selected based on their weight ratio. Depending on the polymer type, this simulation cell contains a total of around 1100 atoms. During the final 1 ns run at 300 K, the dipole moment M is sampled every 10 fs in the NVT ensemble with a definite number of particles (N), volume (V), and temperature (T). The MD results above were imported into the Ovito software for calculation of the hydrogen bonds information.

2.2.3 Thermal conductivity simulation

The thermal conductivity was calculated by the nonequilibrium molecular dynamics (NEMD) simulations. [S9,10] In order to establish a temperature gradient along the z-direction without introducing the coupling between thermostats, vacuum regions were added on each side, and the atoms in the boundary regions along the z-direction were fixed. Then, the Langevin thermostats were applied to the heat source and sink regions as shown in Fig.13(a).

The non-equilibrium simulations were performed for 5 ns to make sure that the system is in steady sate. In steady state, the heat flux Jz along the z-direction is

$$J_z = \frac{1}{2A}\left(\left|\frac{\Delta E_{source}}{\Delta t}\right| + \left|\frac{\Delta E_{sink}}{\Delta t}\right|\right) \quad (6)$$

Here, A is the cross-sectional area in the x-y plane, Δt is the time step, ΔE_{source} and ΔE_{sink} are the amounts of heat added to the heat source and subtracted from the heat sink, respectively. Results show that $\left|\frac{\Delta E_{source}}{\Delta t}\right|$ and $\left|\frac{\Delta E_{sink}}{\Delta t}\right|$ are the same, confirming the symmetry of our system. The value of Jz is 2.73 GW/m2 based on equation 6.

The effective thermal conductivity K_e of the whole semicrystalline region is defined as

$$J_z = K_e \frac{\Delta T}{\Delta L} \quad (7)$$

where ΔT (40 K) is the temperature difference across the fitted region, ΔL is the length of the whole fitted region (120 Å). All the parameters were calculated in the z-direction. Regions used to fit the thermal conductivity are far away enough from the heat bath regions, as shown in Fig. 13(b). The amorphous thermal conductivity K_a was fitted in the 0%-crystallinity configurations, as shown in Fig. 13(c), and the middle region was adopted to fit K_a.

2.2.4 NCl analysis of intermolecular interactions

To further probe intermolecular interactions between dimer model of PI, O-PU, and O-PU/PI. we used noncovalent interaction (NCI) analysis, which is a very powerful visual analysis technique for weak interactions in chemical systems [S11-S13]. It employs isosurfaces of reduced density gradient (RDG) to graphically reveal the main occurrence regions of weak interactions, and distinguishes the interaction types by the colors corresponding to the values of mapped function sign $(\lambda_2)\rho$ on the isosurfaces. It is widely used in theoretical researches of weak interactions for a wide kind of systems, such as intramolecular hydrogen-bond, intermolecular π-π stacking, interaction of metal cation with atomic cluster, ligand-protein binding, interactions in molecular crystal, and so on. Conventionally, van der Waals interactions are identified and shown in green. Stronger interactions are represented by blue (stabilizing and bonding-like) and red (destabilizing and non-bonded). The core idea of the NCI method is to use the RDG-function of a three-dimensional scalar function to reveal the regions where weak interactions mainly occur. The original intention for introducing RDG is to convert density gradient to a dimensionless quantity, the calculations were done within Multiwfn 3.8. RDG is defined as (constant coefficient is ignored) follows:

$$RDG(r) = \frac{1}{2(3\pi^2)^{1/3}} \frac{|\nabla \rho(r)|}{\rho(r)^{4/3}} \tag{8}$$

Where ρ(r) is the eletron density, | ∇ ρ(r) | is the elecron density gradient. It is evident that distinct areas can be differentiated based on varying magnitudes of real space functions. In regions with low electron density, the RDG isosurfaces characterized by small isovalues indicate a region of weak interaction.

2.2.5 Density functional theory (DFT) calculation

Structural optimization: The molecular structure of the monomer model was constructed using GaussView software, necessitating optimization to achieve the most stable conformation with minimal energy. Subsequently, the 6-31G(d) basis set and B3LYP functional were selected to refine the geometric structures of various polymer molecules. Once the molecular conformation was determined, the electrostatic potential, energy level distribution, π–π noncovalent interactions, and hydrogen bond interactions were visualized using GaussView, Multiwfn 3.8, and VMD. The formula for binding energy calculation with BSSE correction using the counterpoise method. The software (Multiwfn 3.8) and parameters for NCI analysis (reduced density gradient isosurface = 0.5 a.u., color scale = $-0.04 < \text{sign}(\lambda_2)\rho < 0.04$ a.u.).

Table S2. The structures of the EPS and homo lumo based on DFT.

Structure	ESP	Homo Lumo	Band Gap (eV)
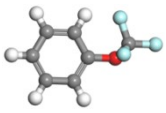 **T-FB**	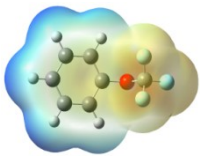	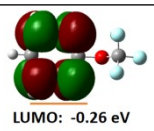 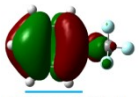	**6.70 eV**
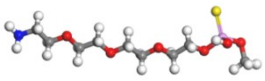 **O-MP**	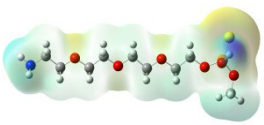	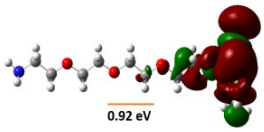 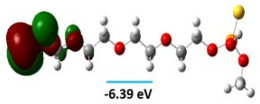	**7.32 eV**

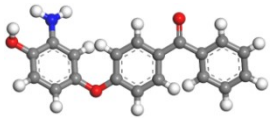 **O-PU**	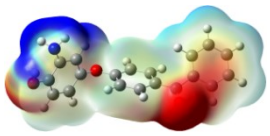	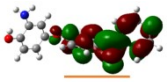 0.80 eV 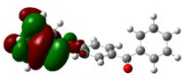 -5.66 eV	**4.86 eV**

Table S3. The chemical structures of the three selected new materials and the free volume simulation results of their composites formed with PI at 25 ℃.

Selected Materials	PI	Blend Composites	Free Volume	Binding Energy (MJ/mol)
 T-FB	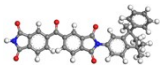	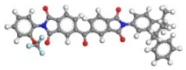	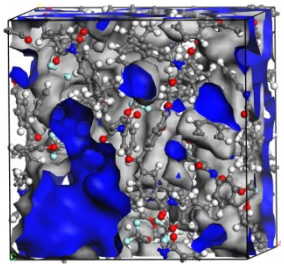 Free Volume: 6957.22 Å^3	3.26
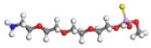 O-MP	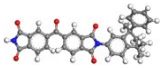	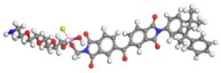	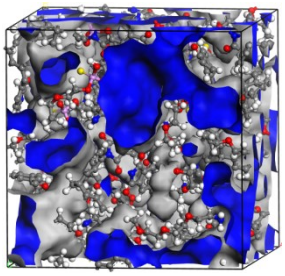 Free Volume: 6710.85 Å^3	5.04
O-PU	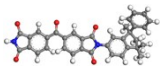	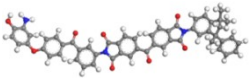	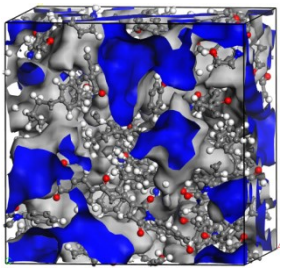 Free Volume: 6363.85 Å^3	6.32

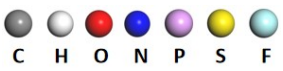

Table S4. The hydrogen bond energy, number of hydrogen bonds, and binding energy of materials.

Materials	Hydrogen bond energy (kJ/mol)	Number of hydrogen bonds	Binding Energy (MJ/mol)
O-PU/O-PU	3.7	64	1.18
O-PU/PI	27.0	483	6.24

3. Film preparation and structural characterization

3.1 Film preparation method

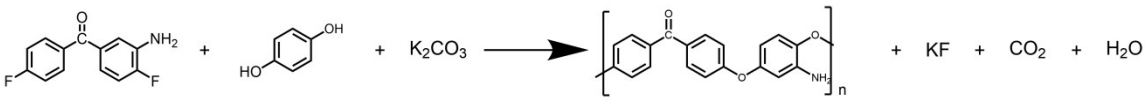

Fig. S1. Schematic of synthesis of O-PU.

3.2 Fourier transform infrared (FTIR) and nuclear magnetic resonance (NMR)

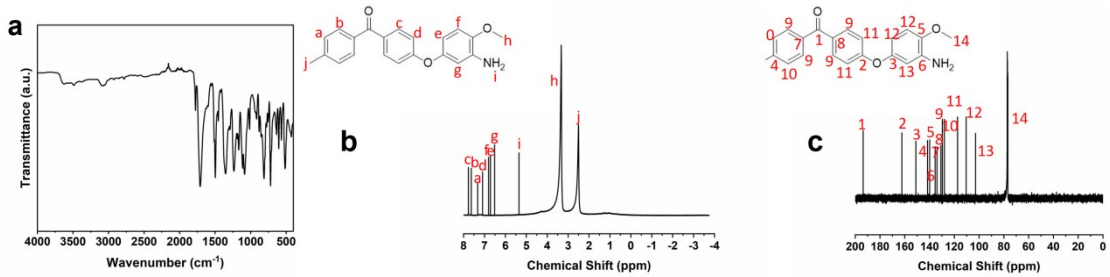

Fig. S2. Characterization of O-PU. (a) FTIR spectra of O-PU, **(b)** ^{1}H NMR spectra of O-PU. **(c)** ^{13}C NMR spectra of O-PU.

3.3 Gel permeation chromatography (GPC)

Table S5. GPC information of O-PU.

M_n (g/mol)	M_w (g/mol)	M_z (g/mol)	PDI (Mw/Mn)
38896	98759	181011	2.54

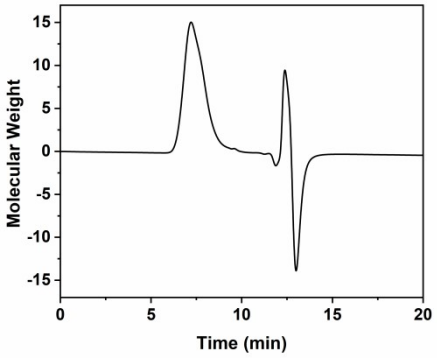

Fig. S3. Molecular weight from GPC of O-PU.

Fig. S4. Film preparation. Photograph of a free-standing film (7×5 cm^2).

3.4 Transmission electron microscopy (TEM) images

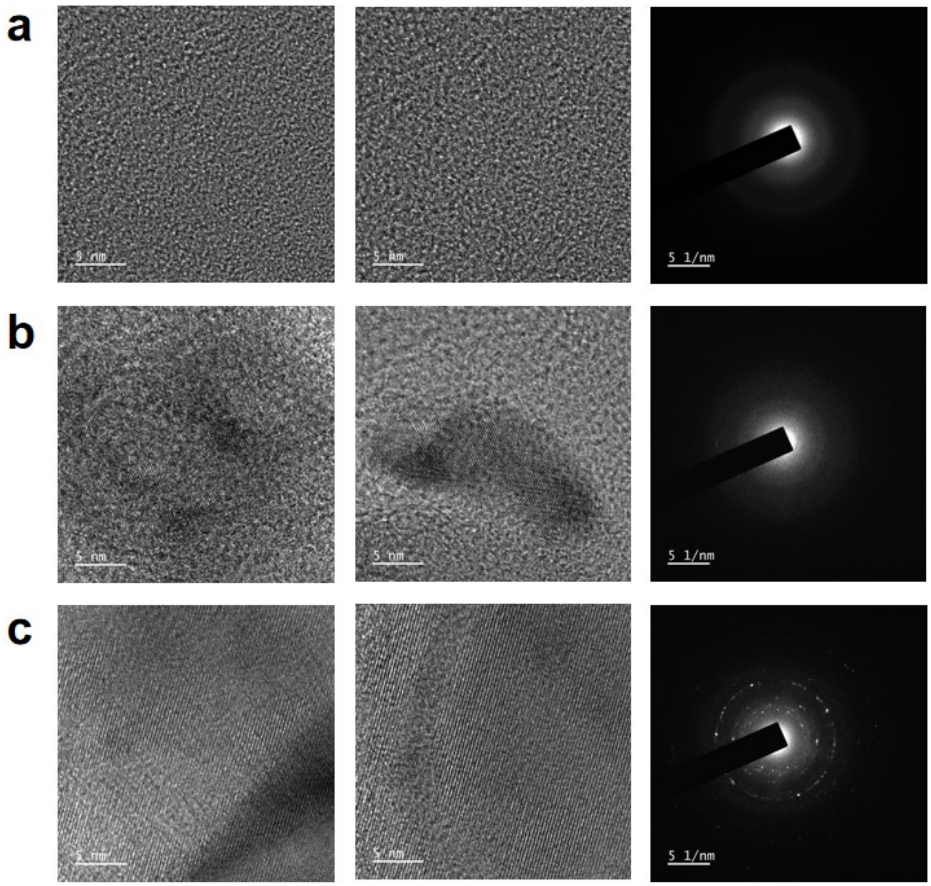

Fig. S5. TEM images of polymer composites. (a) PI. **(b)** O-PU. **(c)** O-PU/PI.

3.5 Atomic force microscopy (AFM) images

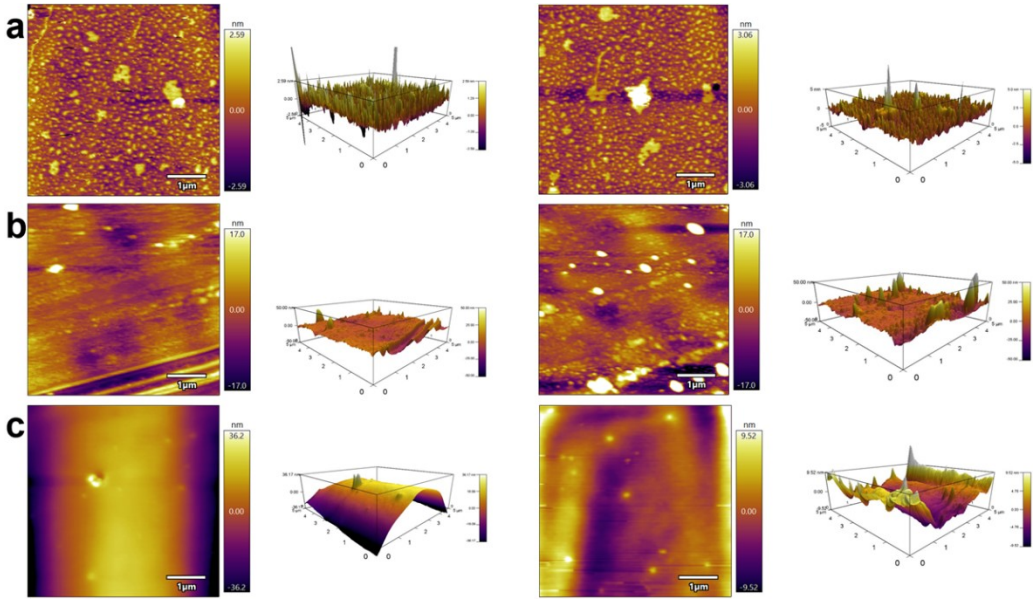

Fig. S6. AFM images of polymer composites. (a) PI. **(b)** O-PU. **(c)** O-PU/PI.

3.6 Scanning electron microscope (SEM) images

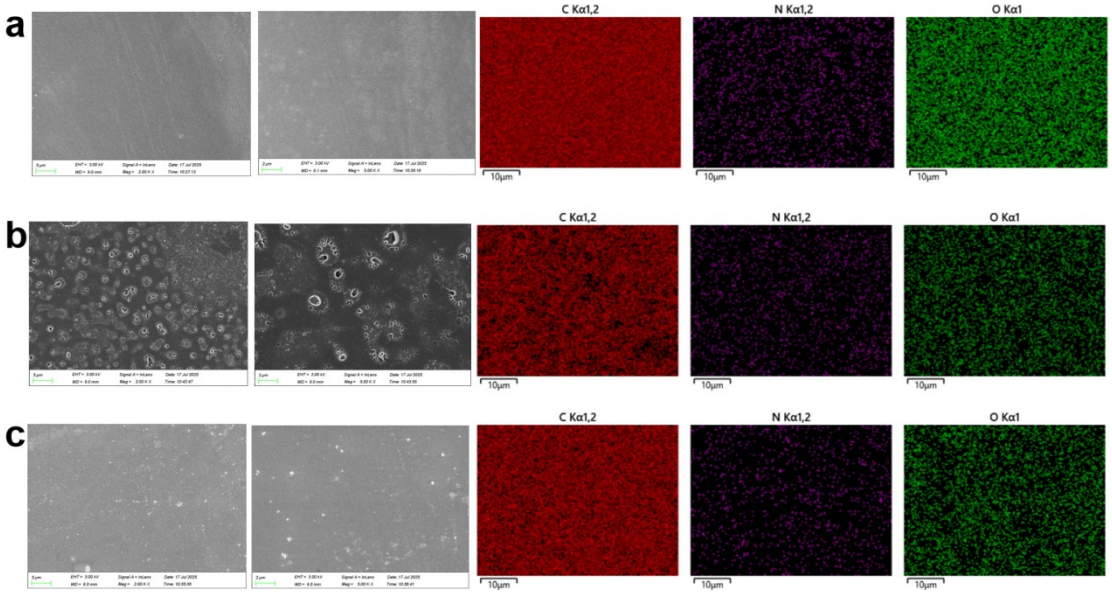

Fig. S7. SEM images of polymer composites. (a) PI. **(b)** O-PU. **(c)** O-PU/PI.

4. Properties of polymer films

4.1 Dielectric constant and dielectric loss

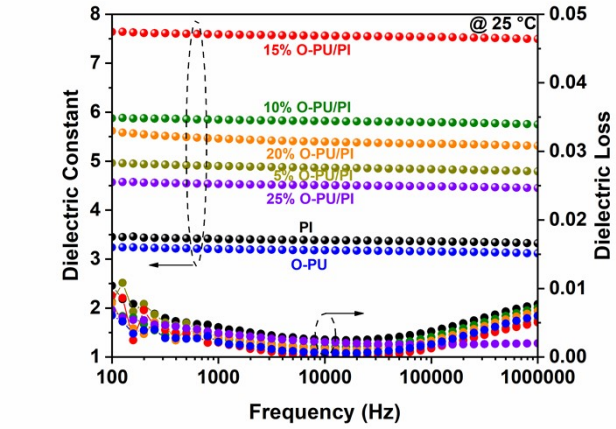

Fig. S8. Dielectric properties. Dielectric spectra of PI, O-PU and O-PU/PI with different loadings of O-PU at various frequencies at 25 ℃.

.

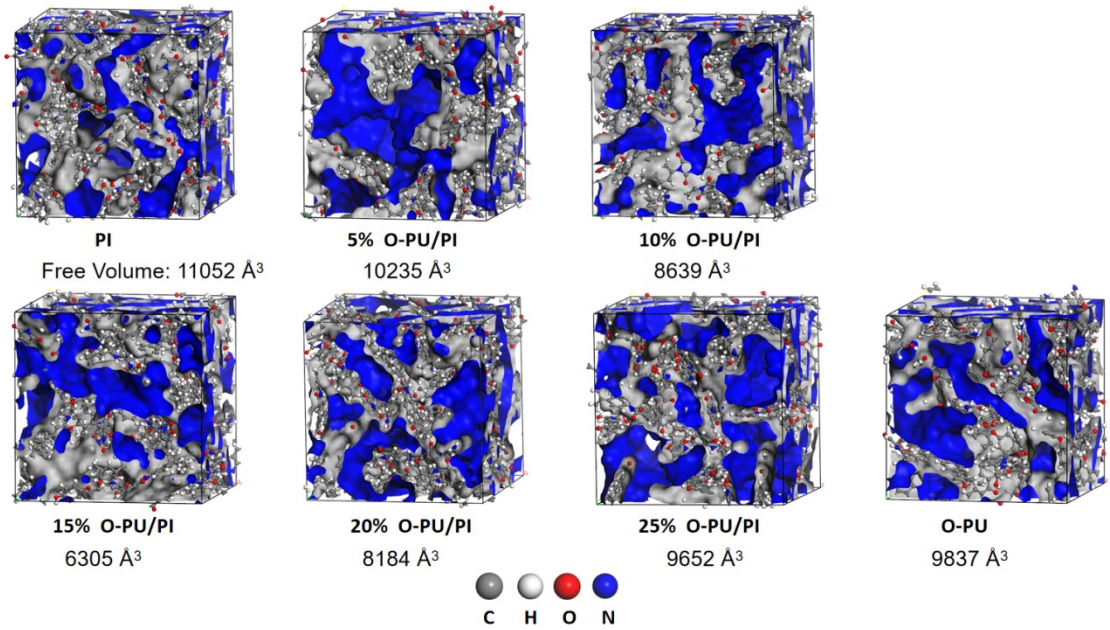

Fig. S9. The free volume simulation results of O-PU/PI with various loadings of O-PU at 25 ℃.

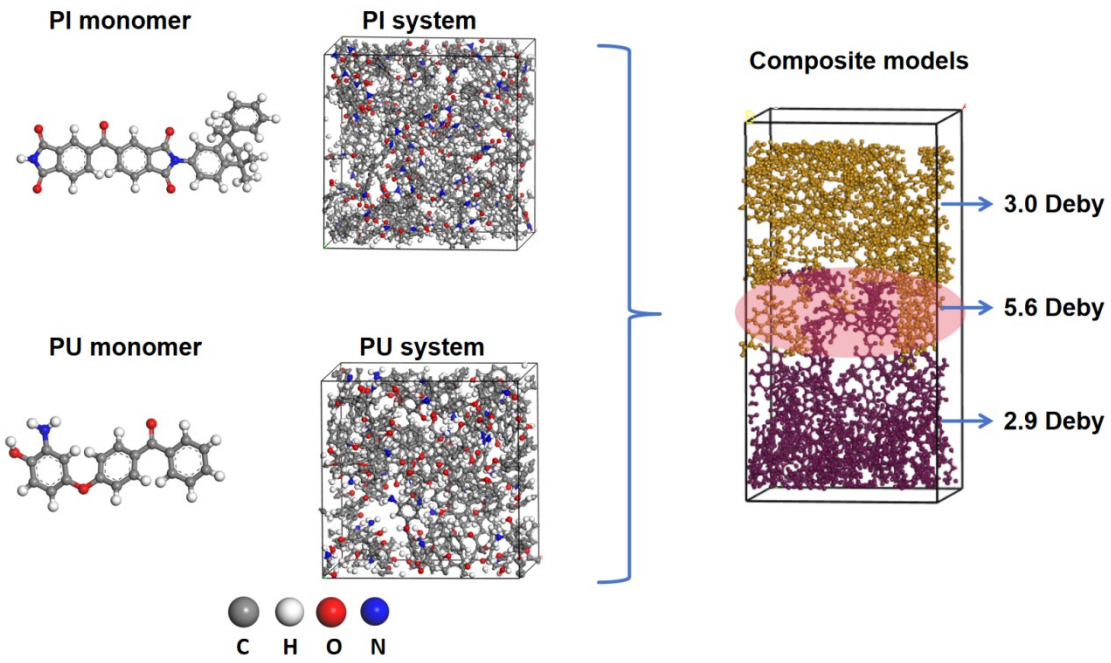

Fig. S10. Effective dipole moments of neat PI, neat O-PU, and the O-PU/PI interface calculated from MD simulations. For visualization convenience, in the blending model, we set PI to yellow and O-PU to brown.

4.2 Leakage current density

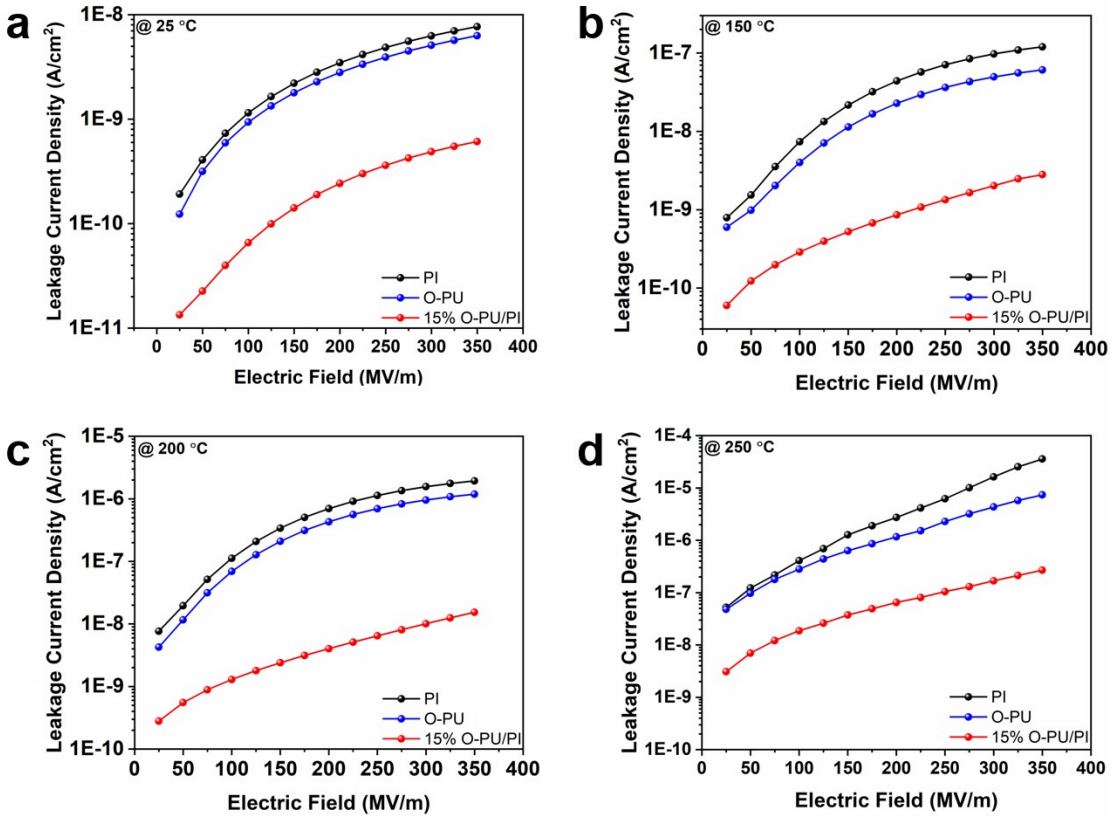

Fig. S11. Leakage current density. Leakage current density of PI, O-PU and 15% O-PU/PI under different electric fields. (a) at 25 ℃. **(b)** 150 ℃. **(c)** 200 ℃. **(d)** 250 ℃.

4.3 Electronic bandgap

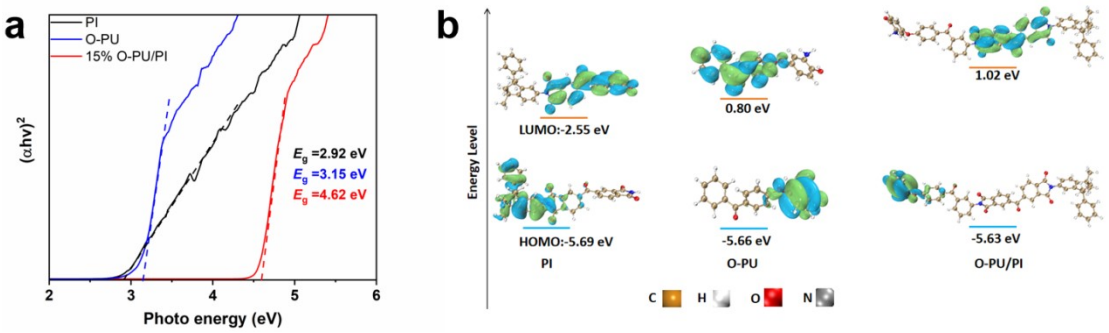

Fig. S12. Bandgap analysis. (a) UV-vis absorption spectra of pure PI, O-PU, and 15% O-PU/PI composite films. **(b)** Bandgap of PI, O-PU, and 15% O-PU/PI.

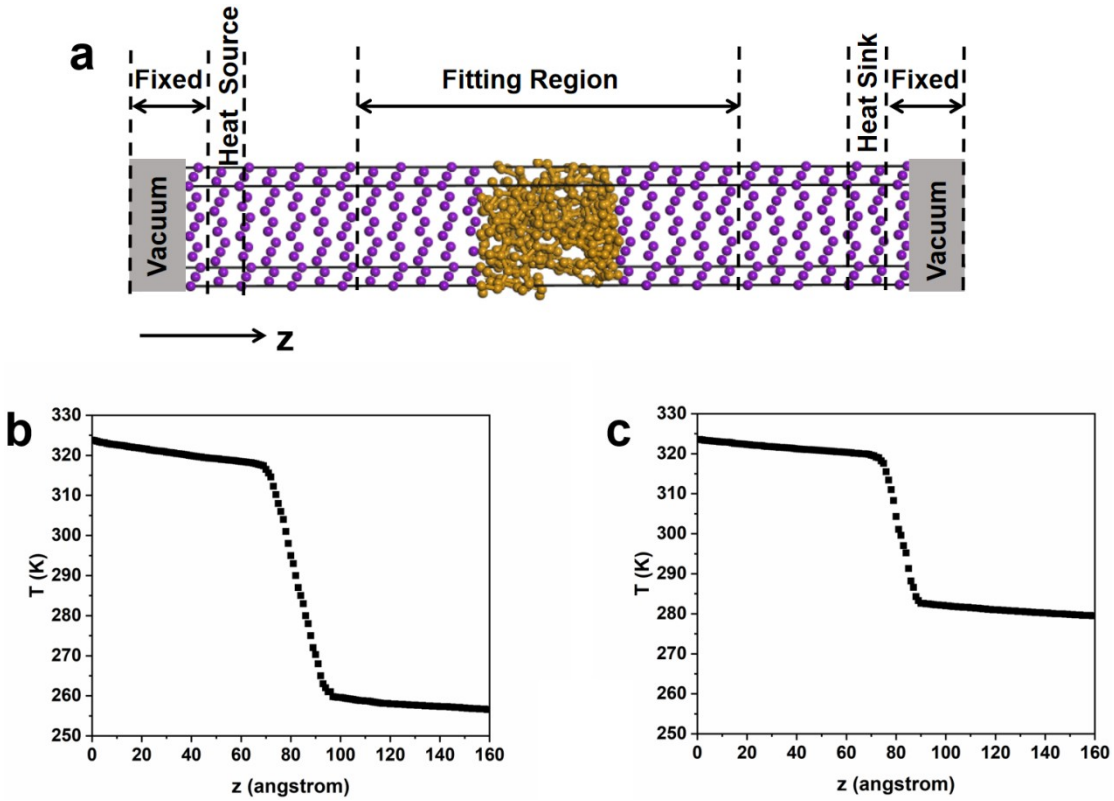

Fig. S13. (a) Schematic diagram for nonequilibrium molecular dynamics (NEMD) simulations. Atoms in crystalline regions are in purple, while atoms in the amorphous regions are in yellow. Vacuum regions were added on each side along the z-direction. Atoms in the boundary regions were fixed. Heat source and sink were applied in the following regions. Fitting region was chosen far away enough from the thermostats. **(b)** A typical temperature profile in the NEMD simulation and the fitting parameter for effective thermal conductivity in semicrystalline O-PU/PI. **(c)** A typical temperature profile in the NEMD and the fitting line for amorphous thermal conductivity in 0% crystallinity PI.

4.4 Thermogravimetric analysis (TGA) and differential scanning calorimetry (DSC)

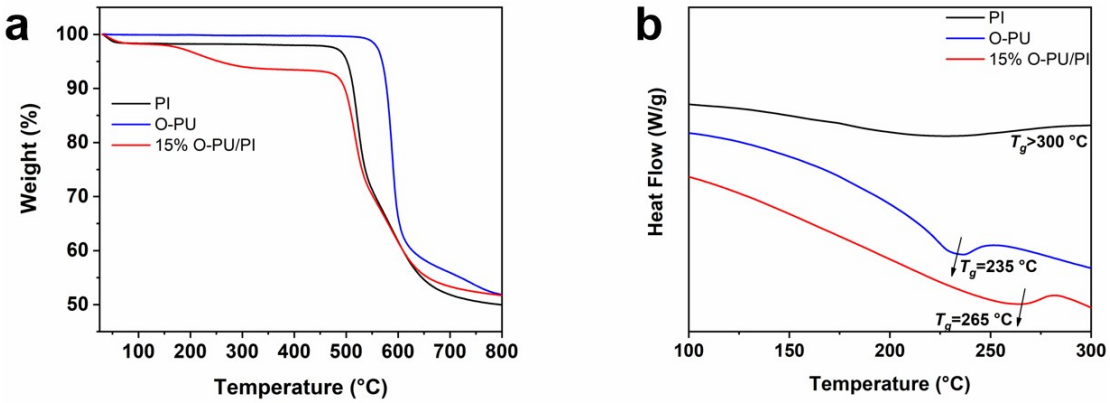

Fig. S14. Thermal properties. (a) TG and (**b**) DSC of PI, O-PU, and 15% O-PU/PI.

4.5 Strain-stress of polymer films

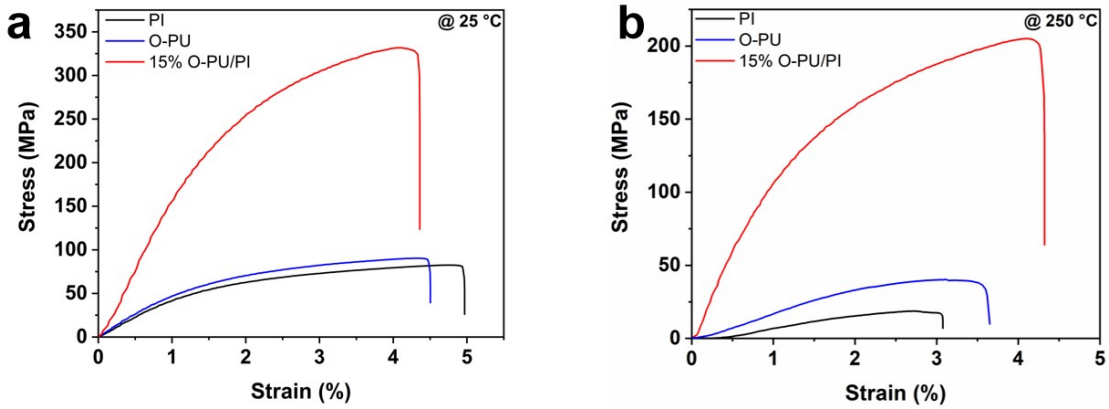

Fig. S15. Strain-stress of PI, O-PU, and 15% O-PU/PI at **(a)** 25 ℃, **(b)** 250 ℃.

4.6 Young's modulus of polymers

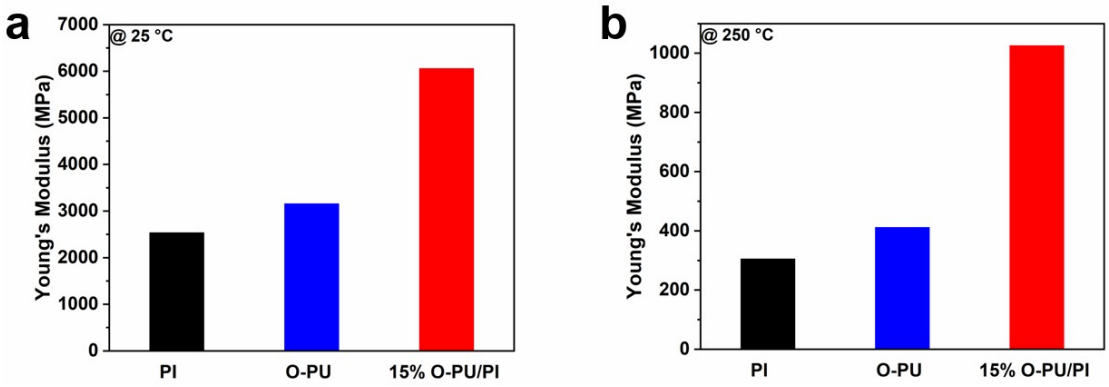

Fig. S16. Young's modulus of PI, O-PU, and 15% O-PU/PI at **(a)** 25 ℃, **(b)** 250 ℃.

4.7 WeiBull of polymer films

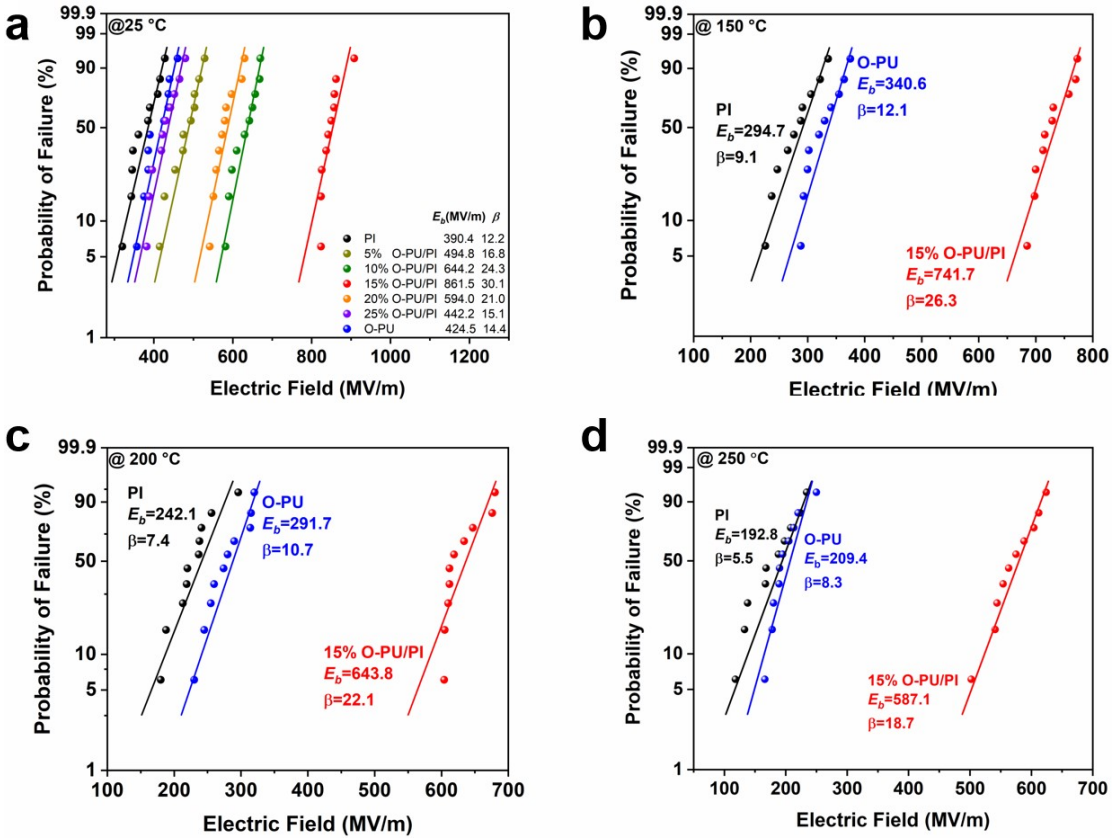

Fig. S17. WeiBull of PI, O-PU, and O-PU/PI **(a)** 25 ℃. **(b)** 150 ℃. **(c)** 200 ℃. **(d)** 250 ℃. (n = 10 specimens per condition)

4.8 P-E loops of polymer films.

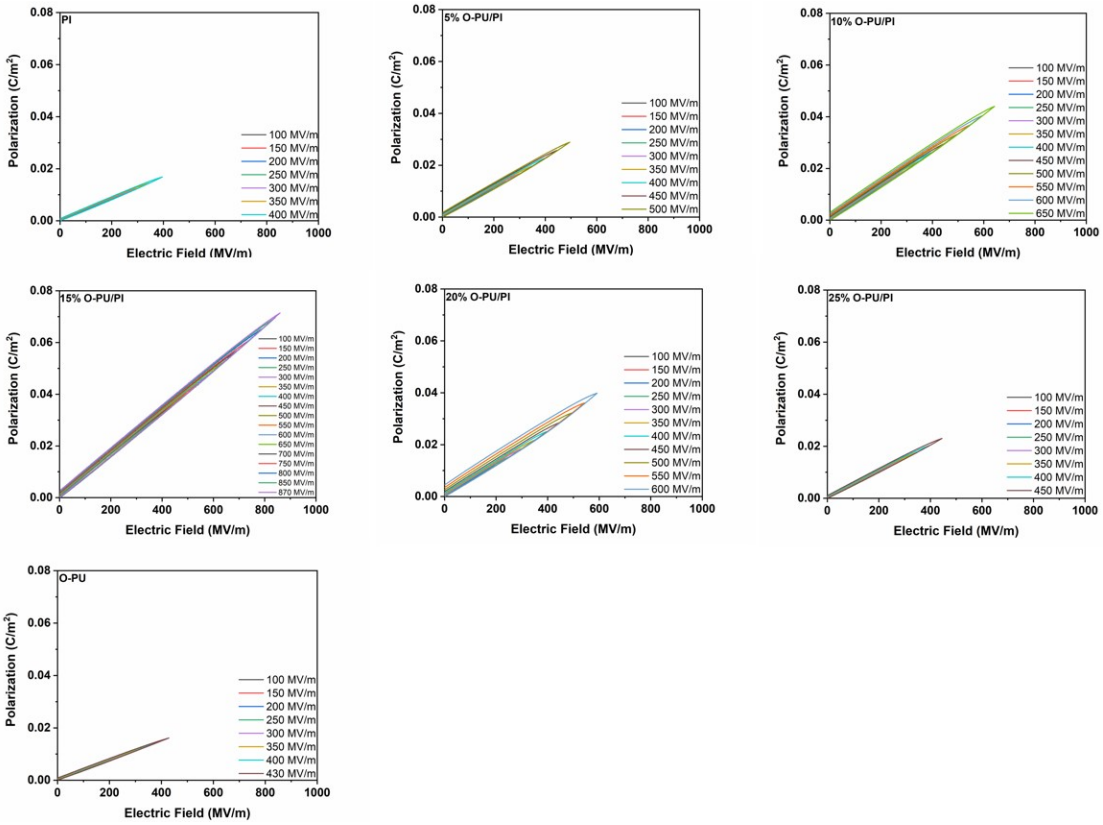

Fig. S18. *P-E* loops. *P-E* loops of PI, O-PU, and O-PU/PI with different weight ratio at 25 ℃.

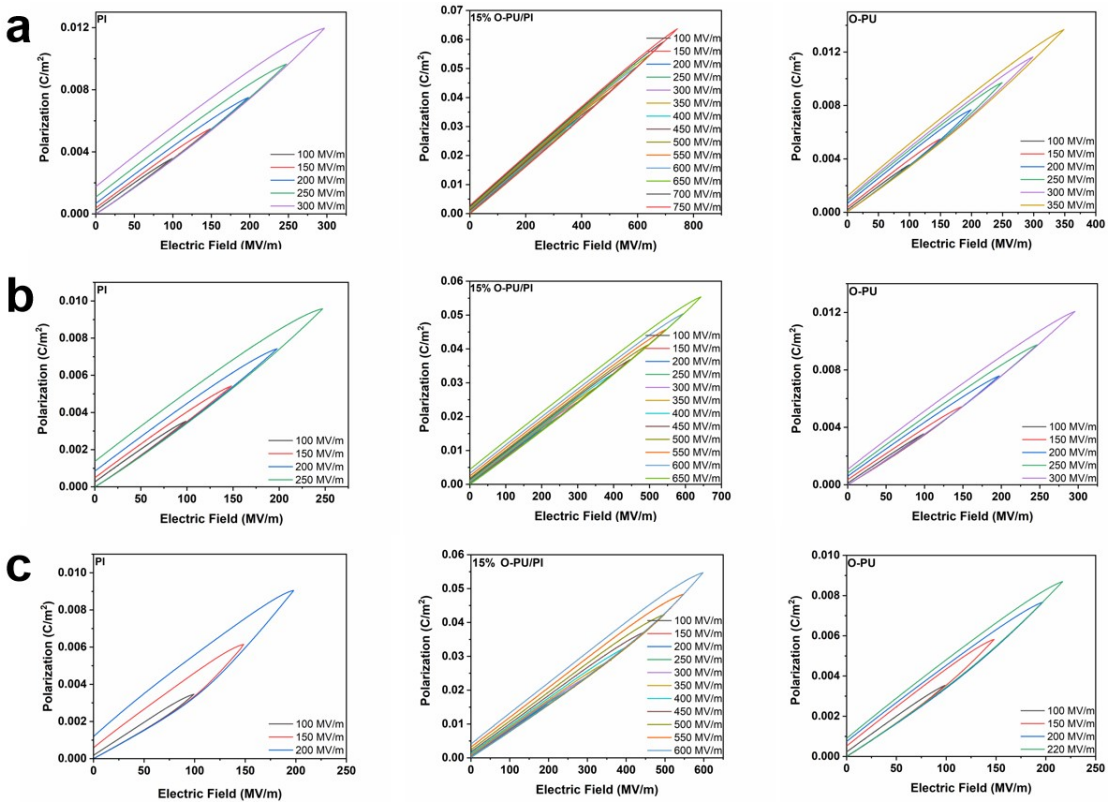

Fig. S19. *P-E* loops. *P-E* loops of PI, O-PU, and 15% O-PU/PI at **(a)** 150 ℃. **(b)** 200 ℃. **(c)** 250 ℃.

4.9 Discharged energy density and charge-discharged efficiency of polymer films

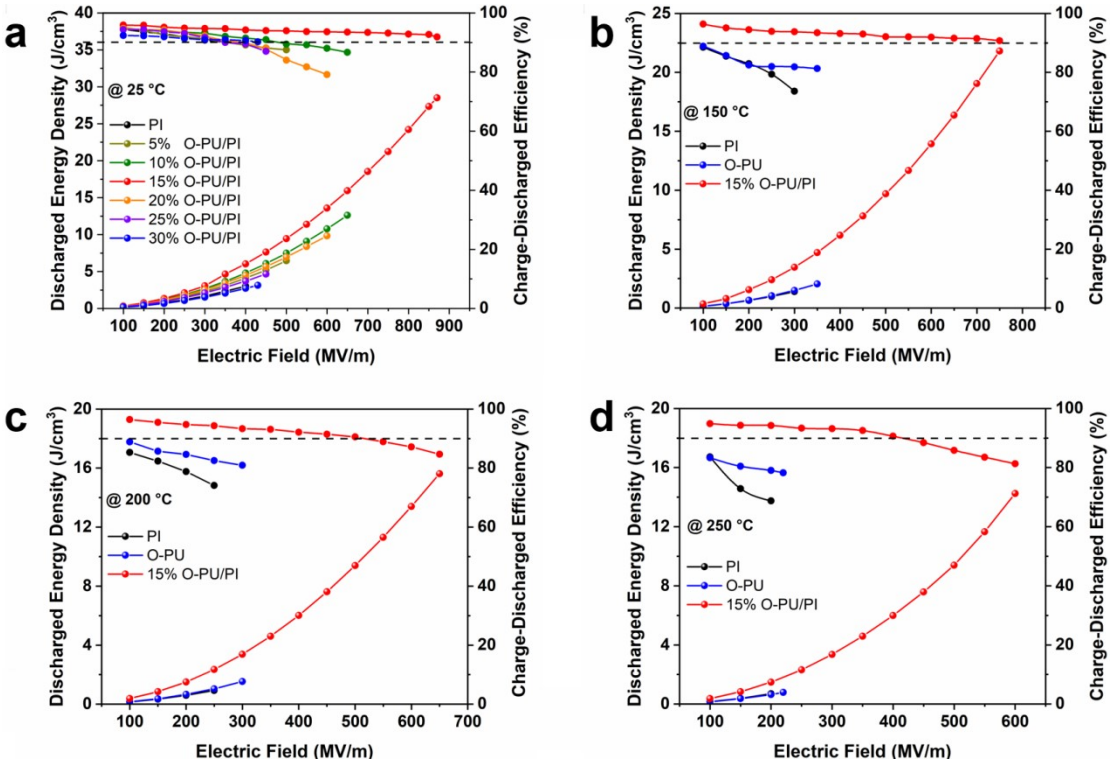

Fig. S20. Discharged energy density and charge-discharged efficiency of PI, O-PU, and O-PU/PI at **(a)** 25 ℃. **(b)** 150 ℃. **(c)** 200 ℃. **(d)** 250 ℃.

4.10 Reliability of polymer films

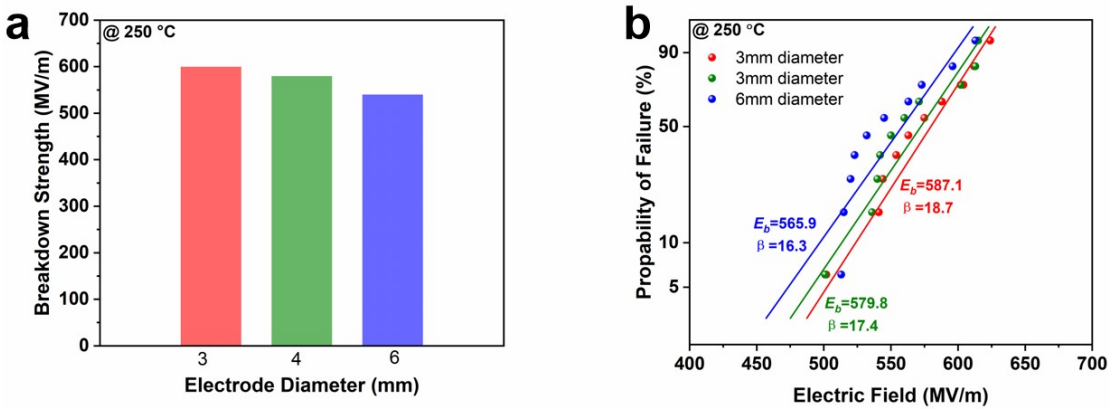

Fig. S21. Reliability of polymers. (a) Breakdown strength and **(b)** Weibull distribution for different electrode diameters of 15% O-PU/PI measured at 250 ℃.

References

[S1] D. Ai, H. Li, Y. Zhou, L. L. Ren, Z. B. Han, B. Yao, W. Zhou, L. Zhao, J. M. Xu, Q. Wang, Tuning nanofillers in in situ prepared polyimide nanocomposites for high-temperature capacitive energy storage. *Adv. Energy Mater.* **10**, 1903881 (2020). doi:10.1002/aenm.201903881

[S2] Z. W. Li, H. M. Qin, J. H. Song, M. Liu, X. L. Zhang, S. Wang, C. X. Xiong, Polyimide nanodielectrics doped with ultralow content of MgO nanoparticles for high-temperature energy storage. *Polymers* **14**, 2918 (2022). doi:10.3390/polym14142918

[S3] Z. Q. Wu, Y. W. Peng, Y. Song, H. Y. Liang, L. Gong, Z. G. Liu, Q. Y. Zhang, Y. H. Chen, Polyimide dielectrics with cross-linked structure for high-temperature film capacitors. *Mater. Today Energy* **32**, 101243 (2023). doi:10.1016/j.mtener.2022.101243

[S4] H. Li, L. L. Ren, D. Ai, Z. B. Han, Y. Liu, B. Yao, Q. Wang, Ternary polymer nanocomposites with concurrently enhanced dielectric constant and breakdown strength for high-temperature electrostatic capacitors. *InfoMat* **2**, 389-400 (2020). doi:10.1002/inf2.12043

[S5] C. Chen, J. W. Xing, Y. Cui, C. H. Zhang, Y. Feng, Y. Q. Zhang, T. D. Zhang, Q. G. Chi, X. Wang, Q. Q. Lei, Designing of ferroelectric/linear dielectric bilayer films: an effective way to improve the energy storage performances of polymer-based capacitors. *J. Phys. Chem. C* **124**, 5920-5927 (2020). doi:10.1021/acs.jpcc.9b11486

[S6] R. Dong, V. Ranjan, M. B. Nardelli, J. Bernholc, Atomistic simulations of aromatic polyurea and polyamide for capacitive energy storage. *Phys. Rev. B* **92**, 024203 (2015). doi:10.1103/PhysRevB.92.024203

[S7] B. Zhang, X. Chen, W. C. Lu, Q. M. Zhang, J. Bernholc, Morphology-induced dielectric enhancement in polymer nanocomposites. *Nanoscale* **13**, 10933 (2021). doi:10.1039/D1NR00165E

[S8] J. F. Li, W. Jiang, Y. Gao, Synergistic P-N charring agents to enhance flame retardancy of ethylene-vinyl acetate (EVA): Insights from experimental and molecular dynamic simulations. *Polym. Degrad. Stab*. **218**, 110570 (2023). doi:10.1016/j.polymdegradstab.2023.110570

[S9] P. K. Schelling, S. R. Phillpot, P. Keblinski, Kapitza conductance and phonon scattering at grain boundaries by simulation. *J. Appl. Phys*. **95**, 6082–6091 (2004). doi:10.1063/1.1702100

[S10] C. Oligschleger, J. C. Schon, Simulation of thermal conductivity and heat transport in solids. *Phys. Rev. B* 59, 4125–4133 (1999). doi:10.1103/PhysRevB.59.4125

[S11] T. Lu, F. W. Chen, Multiwfn: A multifunctional wavefunction analyzer. *J. Comput. Chem* **33**, 580-592 (2012). doi:10.1002/jcc.22885

[S12] T. Lu, Q. X. Chen, Independent gradient model based on Hirshfeld partition: A new method for visual study of interactions in chemical systems. *J. Comput. Chem* **43**, 539-555 (2022). doi:10.1002/jcc.26812

[S13] C. Lefebvre, G. Rubez, H. Khartabil, J. C. Boisson, J. Contreras-García, E. Hénon, Accurately extracting the signature of intermolecular interactions present in the NCI plot of the reduced density gradient versus electron density. *Phys. Chem. Chem. Phys* **19**, 17928-17936 (2017). doi:10.1039/c7cp02110k